# Dual-resonator kinetic inductance detector for distinction between signal and $1/f$ frequency noise

N. Foroozani,[1,2,*] B. Sarabi,[1] S. H. Moseley,[3,‡] T. Stevenson,[3] E. J. Wollack,[3] O. Noroozian,[3] and K. D. Osborn[1,4,5,†]

[1] *Laboratory for Physical Sciences, University of Maryland, College Park, Maryland 20740, USA*
[2] *Department of Physics, University of Maryland, College Park, Maryland 20742, USA*
[3] *NASA Goddard Space Flight Center, Greenbelt, Maryland 20771, USA*
[4] *Joint Quantum Institute, University of Maryland, College Park, Maryland 20742, USA*
[5] *Quantum Materials Center, University of Maryland, College Park, Maryland 20742, USA*

(Received 19 May 2023; accepted 14 December 2023; published 8 January 2024)

Astronomical kinetic inductance detectors (KIDs), similar to quantum information devices, experience performance-limiting noise from materials. In particular, $1/f$ (frequency) noise arises from two-level system defects (TLSs) in the circuit dielectrics and material interfaces and can be a dominant noise mechanism. Here, we present a dual-resonator KID (DuRKID), which is designed for improved noise-equivalent power relative to standard $1/f$-noise-limited KIDs. In this study we present the DuRKID schematic, a fabricated example, our first measurement results, a theoretical model including $1/f$ noise, and a system-noise model containing additional noise sources. The circuit consists of two superconducting resonators sharing an electrical capacitance bridge of four capacitors, each of which hosts TLSs. The device is intended to operate using hybridization of the modes, which causes TLSs to either couple to one mode or the other, depending upon which capacitor they reside in. In contrast, the signal will affect a resonator inductance and, due to mode hybridization, this causes correlated frequency changes in both modes. Therefore, one can better distinguish the photon signal from the TLS frequency noise. To achieve hybridization, a TiN inductor is current biased to allow tuning of one bare-resonator mode into degeneracy with the other. Measurements show that the resonator modes hybridize as expected. The inter-resonator coupling and unintentional coupling of the two resonators to transmission lines are also characterized in measurements. A quantum information-science model allows device-parameter extraction from experimental data and a $1/f$ noise analysis with uncorrelated noise. A system-noise analysis of the DuRKID, with comparisons to standard KIDs, is performed with generation-recombination noise and amplifier noise. The study reveals that the DuRKID can exhibit a large performance advantage over TLS-limited KID detectors.

DOI: 10.1103/PhysRevApplied.21.014009

## I. INTRODUCTION

Kinetic inductance detectors (KIDs) [1–4] for astronomy contain resonators that experience noise that is similar to the noise in qubits for quantum information processing (QIP) [5–9]. For KID-based millimeter and submillimeter-wave astronomical imaging systems [10–12], the signal band of interest contains frequency noise that appears as a strong $1/f$ -like noise spectrum. To achieve the underlying device sensitivity, scan strategies and signal modulation techniques must be implemented to mitigate the influence of noise on the final observational data products [13–15]. More generally speaking, if unaddressed in such applications, the presence of residual low-frequency variations introduces correlated noise that can lead to increased effective noise levels and systematic artifacts that include image striping and amplitude calibration errors. While significant progress has been made over the past two decades in reducing low-frequency noise in KIDs, developing sensitive detectors with lower noise remains the primary technical challenge for many current and future astrophysical observatories [16–18].

The performance in KIDs and qubits is sometimes limited by the same defect type, i.e., a defect commonly named the two-level system (TLS), which resides in dielectrics and at material interfaces within the device. KIDs are perturbed in resonance frequency by the illuminating photon signal [1]; however, TLSs meanwhile induce $1/f$ frequency noise, which causes difficulties in

*nforouzani@lps.umd.edu
†kosborn@umd.edu
‡Current institution: Quantum Circuits, Inc.

 

signal detection [3]. Similarly, in QIP, the qubit transition experiences frequency noise from TLSs [5,19]. This noise necessitates recalibration of pulse-driven qubit logic gates [20,21]. Recent studies of TLS noise mechanisms for KIDs and qubits have shown the importance of a more in-depth understanding of TLSs [5,19,21–23]. Two recent theories explain that the interaction between TLSs is responsible for $1/f$ frequency noise, whereby low-frequency thermally fluctuating TLSs influence high-frequency (near-resonance) TLSs [24,25], which in turn interact with the high-frequency superconducting mode [26,27]. Traditionally, the influence of TLSs in KIDs and qubits is minimized through material choices [28–32] and geometry optimization [4]. While increasing the measurement power lowers the frequency noise from TLSs, it also generates quasiparticles. This leads to the obfuscation of the KID photon signal, because the signal is itself caused by quasiparticles (via illumination of the detector) [33].

Recognizing that practical limitations to frequency noise in KIDs remain, we propose to tackle the problem differently. Here, we describe a detector circuit that can allow one to distinguish photon signal from TLS frequency noise. The circuit uses two resonators coupled with an electrical capacitance bridge and is named a dual-resonator KID (DuRKID). The design allows a shift of an inductor value through a bias current. When operating as a full detector, we imagine this inductor would also shift inductance from illumination, similar to a standard KID. In the DuRKID, the inductance shift causes correlated frequency shifts of both resonator modes. However, in the same device, the TLSs will cause uncorrelated frequency shifts in the resonator modes because high-frequency TLS noise will appear independently in two groups of capacitors. We use established circuit quantum electrodynamics (cQED) analysis to model the circuit, which includes TLSs as a noise source. In Sec. II, we present the DuRKID circuit schematic and fabrication details. Data from the device, including frequency tuning and hybridization, are also shown in this section. In Sec. III, an analysis of the DuRKID is described, with representative TLSs. The analysis is used to extract the dielectric loss and various coupling factors from resonator data. Section IV describes a system-noise analysis of a DuRKID in comparison to a standard KID. We conclude in Sec. V.

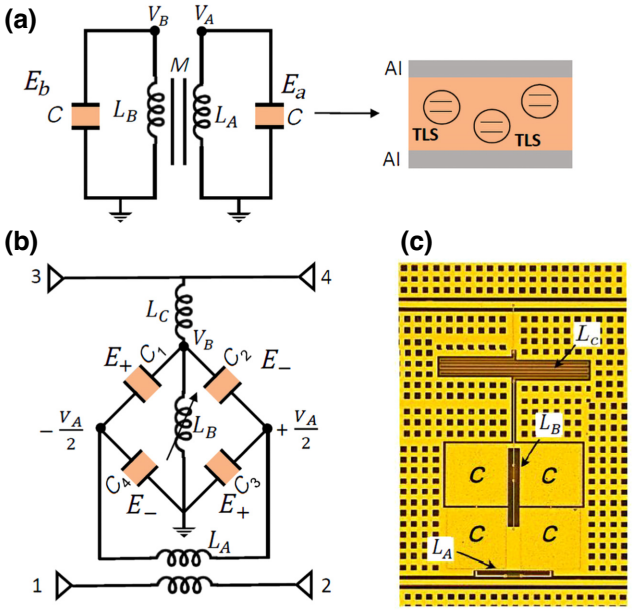


FIG. 1. (a),(b) Resonators with two modes (an extra mode relative to a standard MKID). If the modes are far detuned (in frequency), the modes are effectively decoupled from each other and also experience different TLS noise environments. (a) The standard-coupled resonator circuit. When the two modes are hybridized, TLS noise from both capacitors will equally influence the two resonator modes: $E_a(t) = E_b(t)$ and $E_a(t) = -E_b(t)$. (b) A circuit schematic of the dual-resonator KID (DuRKID). An electrical bridge of nominally equal capacitances ($C_1$–$C_4$) defines the mode, as described below. Spatial resonator modes $A$ and $B$, with voltage components $V_A$ and $V_B$, are hybridized for equal $L_A$ and $L_B$ by stray coupling. For the hybridized mode where $V_A(t)$ and $V_B(t)$ are in phase, the electric field in capacitors 1 and 3 adds $E_+ \propto \langle a + b \rangle$ but in capacitors 2 and 4 the electric fields are out of phase and cancel $E_- \propto \langle a - b \rangle$. For the other hybridized mode, the location of constructive and destructive interference is swapped. The interference of the electric fields gives selective sensitivity of the modes to a TLS, depending on which capacitor hosts the TLS. In this schematic, a dc-bias current applied to port 3 may tune inductance $L_B$. (c) An optical image of the fabricated DuRKID. The materials include Si substrate (black), Al (yellow), TiN (dark red), and a silicon nitride dielectric (obscured).

## II. DEVICE DESIGN, METHOD OF NOISE DISTINCTION, AND MEASUREMENT

TLSs shift the resonator frequency, as does the photon signal, in standard KIDs. The former effectively causes a change in the frequency-dependent dielectric constant and the latter causes an increase in the kinetic inductance of a superconductor [34]. We propose the DuRKID, a device with two specially coupled resonator modes, in contrast to standard KIDs, to improve the noise sensitivity that is hampered by TLS-induced frequency shifts. In the DuRKID, we find that noise from TLSs should be qualitatively different from the signal such that the two are distinguishable and the effective signal sensitivity is improved.

We begin with a discussion of a standard-coupled resonator pair, where $LC$ resonators are nominally of the same frequency (degenerate) without coupling. This reference case is shown in Fig. 1(a), where the resonators are inductively coupled through stray mutual inductance $M$. Alternatively, they could be coupled through a capacitor for the same effect. In the schematic, each bare (uncoupled)

resonance mode frequency, $f_{r,A}$ and $f_{r,B}$, is created by an individual inductor, $L_A$ and $L_B$, respectively. Without resonator coupling, a given TLS in the capacitor of each resonator will couple solely to the field of that resonator and the resonators will act as two separate KIDs. For each mode, one TLS causes a dispersion (frequency shift): $\Delta f_r = (g/(2\pi))^2/(f_{\mathrm{TLS}} - f_{\mathrm{res}})$, where $f_{\mathrm{TLS}}$ is the TLS frequency and $g$ is the coupling between the TLS and the resonator mode. In contrast, when the resonators are set to the same bare frequency of the real device, the coupling will hybridize the modes and standard weakly coupled TLS in a capacitor will interact with both modes through the same coupling term $g$, hence causing correlated noise in the modes. TLSs between the mode frequencies may be especially troublesome. Their frequency drift may cause a correlated drift in both modes. *However, illumination of the intended inductor will also cause a correlated change in the frequencies. Thus, in a standard-coupled resonator pair hybridized modes will exhibit some correlated TLS noise that is not distinguishable from the signal.*

In this work, we study the DuRKID as an alternative KID. To differentiate the TLS noise from the signal, the DuRKID uses an electrical bridge for coupling between two resonator modes [see Fig. 1(b)], which adds a method to distinguish between the illumination signal and the TLS-induced frequency fluctuation noise. As in the standard-coupled resonator circuit, we have two bare (uncoupled) resonance modes, $A$ and $B$, each comprised of an individual inductor, $L_A$ or $L_B$, respectively, but the capacitance bridge of the DuRKID provides four capacitors shared as an electrical bridge by the resonators. The capacitors are nominally equal such that both modes access the same nominal capacitance. The coupling according to the figure shows that mode $A$ is intentionally coupled to the transmission line with ports 1 and 2. Similarly, mode $B$ is intentionally coupled to the transmission line with ports 3 and 4. However, when hybridized, each mode is coupled to both transmission lines. To create degeneracy between these bare modes, $L_B$ can be increased using increased dc-bias current bias. For example, by using current injection into port 3, we can decrease the higher mode frequency of the device shown in Fig. 1(b) because the dc-bias current enters inductance $L_B$. In this work, we have not illuminated the device but the tunable inductor has an analogous function, because an increase in illumination could in principle increase the kinetic inductance of the same inductor. Due to this intended future functionality, we consider in theoretical analysis that this inductor is changed by illumination.

As mentioned above, the bridge-coupled resonator pair acts differently than a standard-coupled resonator pair. A TLS in a bridge of the capacitor is equally shared by both modes before hybridization. However, once hybridized, one $E$-field mode amplitude is zero in two of the four capacitors. Likewise, the amplitude becomes zero in the other two capacitors for the other hybridized mode. *Thus, a given TLS will only frequency shift (disperse) one of the hybridized modes in a bridge-coupled resonator. In contrast, a change in the frequency from illuminating photons will cause a correlated shift to both modes such that the signal is qualitatively different than TLS noise and thus the signal might be straightforwardly separated from this noise.*

### A. Fabrication and measurement

We have chosen a lumped-element capacitor $C$ for our device design. Related to inductance $L$ and capacitor $C$, lumped-element KIDs were proposed years ago for terahertz KIDs, partially because the lumped $L$ design was found to provide a good method for collecting the created quasiparticles relative to a design that would have quasiparticles distributed throughout a cavity-length resonator [35]. Furthermore, a lumped-element $L$ design has recently been used for millimeter-wave astronomy [36]. Our fabricated design serves as a proof of concept, utilizing $SiN_x$ parallel-plate capacitors, which are compact compared to capacitors that utilize the substrate or silicon-on-insulator- (SOI) based dielectric. While lower-noise capacitors could be used in the future, our fabricated design merely demonstrates one approach.

Many DuRKIDs are fabricated together on a high-resistivity ($> 20\ \mathrm{k\Omega\,cm}$) silicon wafer. A single fabricated DuRKID is shown in Fig. 1(c). There are three DuRKIDs per chip and the physical layout of a chip is shown in Fig. 2(a). Note that the center DuRKID is device 2 and that its orientation matches that of Figs. 1(b) and 1(c). Devices 1 and 3 are rotated by 180° relative to device 2 and they are biased in parallel, unlike device 2. The base superconducting layer is an Al/TiN bilayer, consisting of 250-nm-thick Al on top of 15-nm-thick TiN. The bilayer is patterned followed by the removal of the Al to leave the TiN bare in certain locations to provide kinetic inductances $L_{kA}, L_{kB}$, and $L_{kC}$ as part of the total inductances $L_A, L_B$, and $L_C$, respectively. The dielectric layer in the capacitor bridge is a high-density silicon nitride ($SiN_x$) film with a nominal thickness of 275 nm, deposited using PECVD [37]. Via holes in the dielectric are made using $SF_6$ reactive ion etching. A 250-nm sputtered Al film forms the counter electrode of the capacitor bridge. After patterning the counter electrode, excess $SiN_x$ is removed from most of the sample, which allows access to bonding pads on the base layer.

The devices are cooled down to 20 mK in a dilution refrigerator. The transmission data, $|S_{21}|$ and $|S_{43}|$, for all three devices are shown in Fig. 2(b) when $I_b = 0$. The devices are intentionally designed with differing detunings between the two resonator modes at zero bias current, $I_b$. The tunable resonance at zero dc bias was planned at a higher frequency than the nontunable resonance and this feature has been realized in all three devices. The unbiased

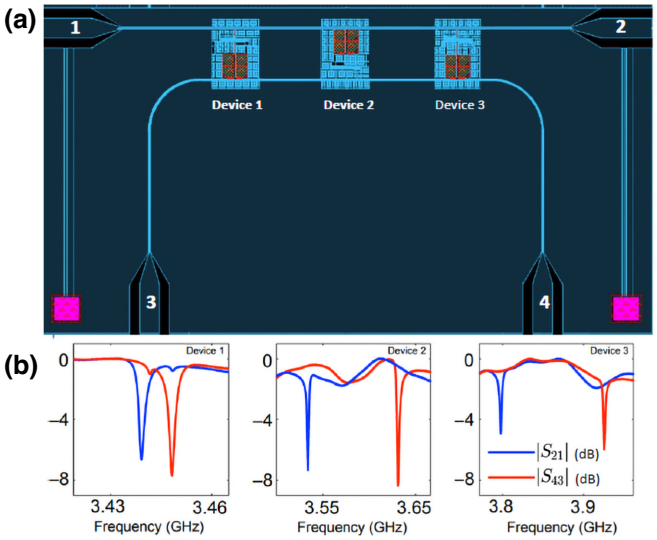


FIG. 2. (a) The device layout of three devices on a chip, with two feed lines for each device. One resonator of each device is tunable, using the nonlinear inductance $L_B$. The $LC$ resonances are mainly defined by a 0.6-nH inductor and trilayer capacitors with $C = 3.14$ pF, containing a 275-nm-thick silicon nitride dielectric film. (b) The measured transmission $|S_{21}|$ and $|S_{43}|$ for devices 1, 2, and 3 at $I_b = 0$.

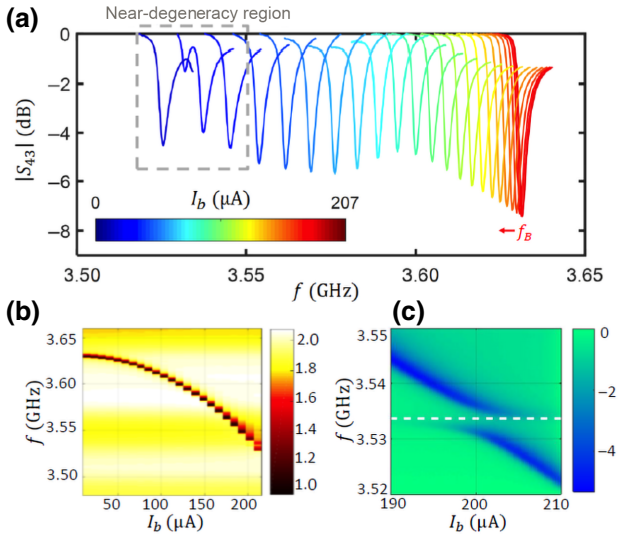


FIG. 3. The data on device 2. The transmission spectra, $|S_{43}|$, of a tunable resonator with an applied bias current up to 210 μA, measured at 20 mK. (a) Each color represents one $|S_{43}(f)|$ trace at a separate dc bias. The frequency of the resonator $B$, as shown by $S_{43}$, shifts down from 3.635 GHz to 3.52 GHz, i.e., by 120 MHz, when the minimum bias is applied for full hybridization. (b) A $S_{43}(f, I_b)$ plot that shows the resonance frequency as a function of the bias over the applied current range $I_b$. (c) The measured transmission $|S_{43}|$ of device $B$ versus the frequency $f_B$ and bias current $I_b$ near degeneracy shows an avoided crossing due to hybridization with the fixed mode at $f_A = 3.533$ GHz. From the analysis, a coupling of $\Omega_{AB}/2\pi = 5.1$ MHz has been obtained.

detuning between two modes for each dual resonator, i.e., for devices 1–3, is measured at $\delta_1 = 9$ MHz, $\delta_2 = 97$ MHz and $\delta_3 = 128$ MHz, respectively. As intended, the dc bias allows all three devices to reach degeneracy with the bias current and for device 3 the tuning required for degeneracy (approximately 128 MHz) is large but is enabled by a large kinetic inductance change from the nominal inductance per square of 56 pH. The fractional frequency tuning $\delta f_r/f_r = 3.5\%$ is approximately an order of magnitude higher than achieved with a magnetic-field tuned coplanar-waveguide resonator [38].

Device 2 transmission data $|S_{43}|$ are shown in two different plots in Figs. 3(a) and 3(b), where Fig. 3(a) shows the resonance spectra in curves at different bias currents and Fig. 3(b) clearly shows the resonance frequency as a function of the bias current. The applied bias current shifts the higher mode toward the lower resonance and the tunable resonator disappears at a bias $I_{b,\max} = 210$ μA, indicating a change to the normal state, likely at the wiring vias. Although most of the geometric inductor length within each resonator is provided by Al, the kinetic inductance $L_{kA}$ and $L_{kB}$ comprise approximately 85% of the total inductance $L_A$ and $L_B$. At temperatures much lower than the superconducting critical temperature $T_c$, the nonlinear response of $L_k$ to $I_b$ can be expanded as $L_k(I_b) = L_k(0)(1 + (I_b/I')^2 + \cdots)$, where $I'$ sets the scale of nonlinearity. By considering up to quadratic order in $L_k(I_b)$, we extract $I' = 789$ μA from a fit to $L_{kB}$ (See Fig. 9 in Appendix A).

The $|S_{43}|$ at different $I_b$ [given in Fig. 3(c)] shows an avoided crossing due to hybridization with the $A$ mode. The operation of the device is intended for full hybridization, which occurs at $I_b \approx 202$ μA in this device. From this bias current, one can simultaneously measure the two resonances using two fixed-frequency sources. These are the tones that are necessary for operating the DuRKID as intended.

We have also measured the cross-coupling from the input port of one transmission line to the output port of the other, $S_{41}$ and $S_{23}$. The transmission $|S_{41}|$ for degenerate hybridized modes is on the order of $-10$ dB (not shown), indicating some internal loss in the resonators but also good coupling of the resonators to their intended transmission lines.

The capacitors of the bridge are carefully designed in layout to be equal. As a result, the mutual inductance is likely the dominant stray coupling mechanism. We note that the splitting from mode coupling must be larger than other line widths for the device to operate as intended. To further analyze the data quantitatively, we have fitted the transmission data, $S_{21}$ and $S_{43}$, to the two-resonator model, where the fitting procedure is explained in Appendix A. From Fig. 3(c), we have obtained the

inter-resonator coupling of $\Omega_{AB}/2\pi = 5.1$ MHz. This coupling agrees, within a factor of 2, with the simulated value. We then use this as a fixed parameter in the device model for a later part of the fitting procedure. We fit both standard transmission data, $S_{21}$ and $S_{43}$, at the same time for the start of the fitting procedure. From this, we extract the internal $Q$ factor of 2750 and 3100 for resonators $A$ and $B$, respectively. When viewed as a material loss tangent, $\tan\delta = 1/Q_i = (3.4 \pm 0.2) \times 10^{-4}$ and the value of this loss matches our expectation for the recipe of PECVD $SiN_x$ that we have used. This loss tangent is lower than that of $AlO_x$ barriers in large-area Josephson junctions by approximately an order of magnitude [21,37]. In other work, SOI is used for higher-$Q$-factor resonators [39,40]. This dielectric type is advantageous for KIDs due to its low loss characteristics, resulting in low noise from TLSs.

We have observed unintended leakage (crosstalk) between the two different feed lines at $|S_{14}| \sim 10^{-4}$. This small value was measured with the resonators detuned and it corresponds to the stray coupling at the frequency of either the $A$ or $B$ resonator mode. From this, we have extracted the couplings of the resonators to the unintended feed lines as $\kappa_{ax} = \kappa_{bx} \sim 20$ kHz, where we define $\kappa_{ix}$ in Sec. III (for details, also see Appendix B). The leakage will generally produce a negligible change to measurements using two feed lines. However, the two hybridized modes can also be read out with one feed line for the sake of simplicity.

It is worth noting that the DuRKID can be multiplexed. One advantage of standard KIDs is that they can be read out at different frequencies using frequency-division multiplexing using one feed line. This multiplexing has enabled approximately 1000-pixel KID arrays [18]. However, in the present DuRKID design, a dc-bias current must also be applied and it is presently applied through a radio-frequency feed line. To achieve the intended biasing for an approximately 1000-pixel DuRKID array, one can use 32 bias lines that are separate from the feed lines, to bias a column of DuRKIDs using a parallel circuit. The microwave measurement of the full array can then occur in 32 measurements in time from one feed line, where each one uses biases set for one row of DuRKIDs.

## III. cQED MODEL OF TWO RESONATORS COUPLED TO THE SAME TLS

### A. Theoretical model

For a theoretical model of the DuRKID, we use a standard quantum information-science method (cf. Ref. [41]). Figure 4(a) shows the system diagram for the model, which has two resonator modes. Per the layout, we describe each resonator mode with its own two-port transmission line. Both modes are coupled to a TLS noise source. Only one TLS and its coupling are shown but the model generally has many TLSs with different couplings to one hybridized resonator mode and the hybridized mode is generally created from inter-resonator mode coupling $\Omega_{AB}$. $\kappa_A$ and $\kappa_B$ are the coupling rates of resonators $A$ and $B$, respectively, to their intended two-port transmission line. The coupling rates of the resonators to the other (unintended) transmission lines are represented by $\kappa_{Ax}$ and $\kappa_{Bx}$, respectively. In this analysis, we focus on TLSs that are far enough from resonance to not be saturated by the drive field. A coupled TLS pair could cause different qualitative noise spectra (cf. Ref. [19]) but the method of protection is qualitative, such that the interaction of the pair within a capacitor should not matter. Generally, we consider that the resonators are coupled to the $i$th TLS with a resonance coupling constant of $g_i$. We represent TLSs with a spin operator $\sigma_i^z$, using the analogy between TLS theory and a two-state system (with pseudospin-1/2). The Hamiltonian for the system interacting with two transmission lines then has the form

$$\begin{aligned} H_{\rm sys} &= \hbar\omega_A a^\dagger a + \hbar\omega_B b^\dagger b + \sum_{i=1}^{N} \varepsilon_i \sigma_i^z + \sum_{j=1}^{M} \varepsilon_j \sigma_j^z \\ &\quad + \hbar\Omega_{AB}(b^\dagger a + a^\dagger b) \\ &\quad - i\hbar \sum_{i=1}^{N} g_i^{(n)} (\sigma_i^+ (a + b) + \sigma_i^- (a^\dagger + b^\dagger)) \\ &\quad - i\hbar \sum_{j=1}^{M} g_j^{(m)} (\sigma_j^+ (a - b) + \sigma_j^- (a^\dagger - b^\dagger)). \end{aligned} \tag{1}$$

This is similar to the one-cavity Jaynes-Cummings model [42–44], except that ours includes two modes (with operators $a$ and $b$) with many TLSs (with raising and lowering operators $\sigma_i^+$ and $\sigma_i^-$). The $i$th TLS has the energy of $\varepsilon_i = \hbar\omega_{{\rm TLS},i}/2 = \sqrt{\Delta_i^2 + \Delta_{0,i}^2}$, where $\Delta_0$ and $\Delta$ are the tunneling energy and the asymmetry energy in the double-well potential model. The TLS resonance coupling to the resonator field is $g_i = \Delta_{0,i}/(\varepsilon_i) p_i \cos\theta_i \sqrt{\omega/2\epsilon_r\epsilon_0\hbar V}$, where $p_i$ is the magnitude of the dipole moment, $\theta_i$ is the angle between $p_i$ and the applied electric field $\mathbf{E}$, $V$ is the dielectric volume, and $\epsilon_r$ is the relative permittivity [45]. Although a given TLS in a capacitor is equally shared by both modes before hybridization, after hybridization the two-mode fields become $E_+ \propto (a + b)$ and $E_- \propto (a - b)$, which are zero in certain capacitors as mentioned above. It becomes zero in two of the capacitors for one hybridized mode and similarly zero in the other two capacitors of the other hybridized mode. We find that this approximation is valid even for a TLS throughout the eigenmode width. For the two modes, we thus effectively have only the coupling to $N$ TLSs (group $n$) in capacitor pair $C_1$ and $C_3$, and $M$ TLSs (group $m$) in pair $C_2$ and $C_4$. Using a standard theoretical procedure [46] for the resonators $A$ and $B$ interacting with the input and output fields as the heat bath, the

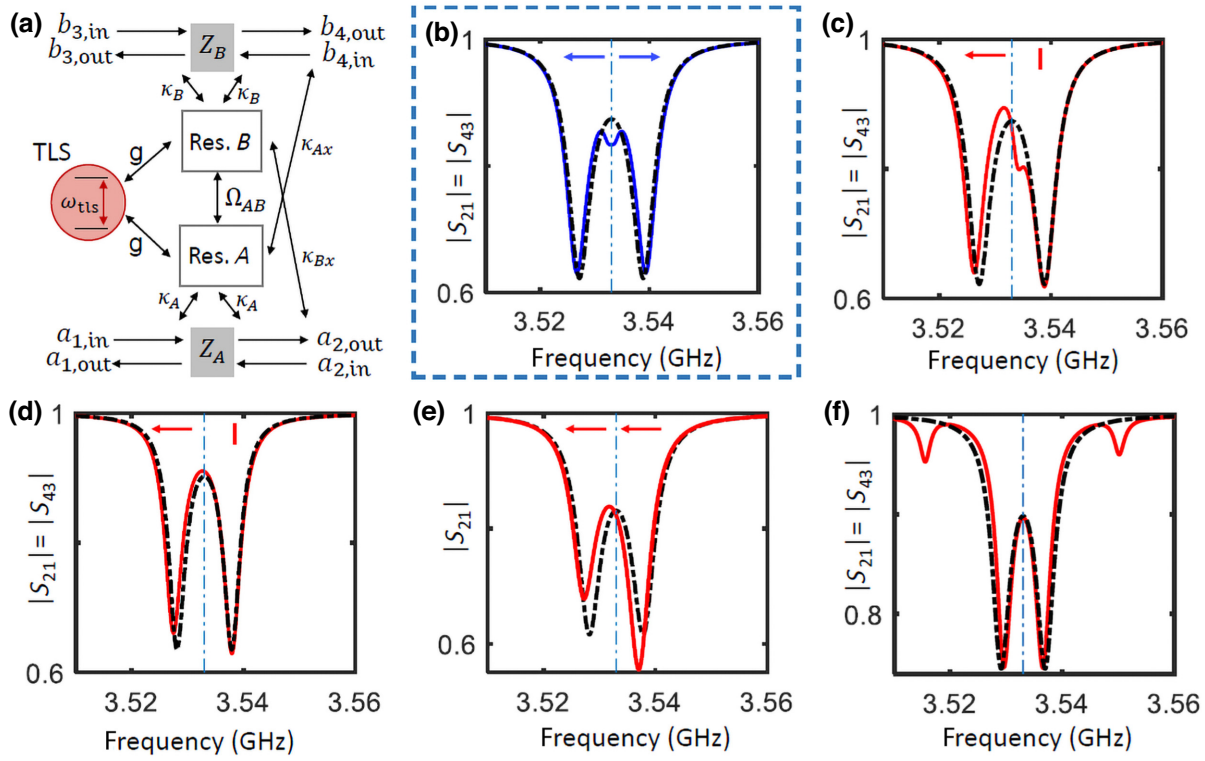


FIG. 4. (a) The theoretical model for the DuRKID, including two resonators, four ports (fully shown), and TLSs (only one TLS shown). In this simulation, the coupling parameters are $\kappa_A/2\pi = \kappa_B/2\pi = 2$ MHz, $\gamma_{TLS}/2\pi = 2$ MHz, $\Omega_{AB}/2\pi = 5$ MHz, and $g/2\pi = 1$ MHz. Resonator $A$ is intentionally coupled to the transmission line of ports 1 and 2, and resonator $B$ to ports 3 and 4. (b)–(f) The transmission analysis for ($1 \rightarrow 2$ or $3 \rightarrow 4$) with $Z_A, Z_B \rightarrow 0$ (zero impedance between transmission line halves). The arrows (red or blue) show the resonator mode frequency (solid curve, transmission minima) change due to the TLS, relative to the mode frequency without the TLS (dashed curve, transmission minima). (b),(c) The single-photon transmission spectrum for two different devices with the same parameters, ($\omega_A/2\pi = \omega_B/2\pi = 3.533$ GHz) with a single degenerate TLS ($\omega_{tls} = \omega_A = \omega_B$). (b) Standard-coupled resonators that are hybridized. Note that the frequency shift (dispersion) occurs equally (correlated) in both modes (blue relative to black minima, also see the blue arrows). (c) DuRKID in intended (hybridized) mode with a TLS. Here, the TLS leaves one of the modes undispersed. (d) DuRKID with a large drive (classical field) amplitude of $\bar{n} = 50$ photons and a TLS frequency of $\omega_{TLS}/2\pi = 3.540$ GHz. Here, the dispersion is present, related to (c), and the TLS is symmetry protected from saturation. Undispersed modes occur in DuRKID due to the absence of fields in certain capacitors according to the symmetry of the hybridized modes [see Fig. 1(b)]. (e) The spectra for the bridge-type resonator device in the presence of an added signal to one inductor [in contrast to other subfigures that use additional TLS(s)]. Here, the hybridization of the modes changes as seen in different resonator transmission amplitudes. The resonator frequency modes shift downward together (as correlated modes), in contrast to the case of a single-TLS perturbation [(c) or (d)]. (f) Spectra with two TLSs, where there is one from each group (where each mainly influences only one of the resonator modes). This case is used in Sec. III B, for analysis with two TLS noise sources. A TLS in each TLS group disperses each hybridized mode but it is distinguishable from the (correlated-mode) signal. In this special case, there is no change of mode hybridization due to the way in which the TLSs oppositely disperse (shift) the resonator modes.

Heisenberg equations of motion can be written as follows:

$$\frac{d}{dt}\langle a\rangle = -i\omega\langle a\rangle = -\frac{i}{\hbar}\langle[a, H_{sys}]\rangle - (\kappa_A+\gamma_A+\kappa_{Ax})\langle a\rangle + \sqrt{\kappa_A}\langle a_{1,in}\rangle + \sqrt{\kappa_A}\langle a_{2,in}\rangle + \sqrt{\kappa_{Ax}}\langle b_{3,in}\rangle + \sqrt{\kappa_{Ax}}\langle b_{4,in}\rangle - \sqrt{\kappa_A\kappa_{Bx}}\langle b\rangle - \sqrt{\kappa_{Ax}\kappa_B}\langle b\rangle, \quad (2)$$

$$\frac{d}{dt}\langle b\rangle = -i\omega\langle b\rangle = -\frac{i}{\hbar}\langle[b, H_{sys}]\rangle - (\kappa_B+\gamma_B+\kappa_{Bx})\langle b\rangle + \sqrt{\kappa_B}\langle b_{3,in}\rangle + \sqrt{\kappa_B}\langle b_{4,in}\rangle + \sqrt{\kappa_{Bx}}\langle a_{1,in}\rangle + \sqrt{\kappa_{Bx}}\langle a_{2,in}\rangle - \sqrt{\kappa_B\kappa_{Ax}}\langle a\rangle - \sqrt{\kappa_{Bx}\kappa_A}\langle a\rangle, \quad (3)$$

where $a_{1,(2),in}, b_{3,(4),in}$ and $a_{1,(2),out}, b_{3,(4),out}$ are the input and output fields. Assuming a coherent-state approximation for photons in resonators $A$ and $B$ coupled to the input and output fields, the transmissions $S_{21}$ and $S_{43}$ are given by $\langle a_{2,out}\rangle/\langle a_{1,in}\rangle$ and $\langle b_{4,out}\rangle/\langle b_{3,in}\rangle$, respectively. The boundary conditions that relate the input and output fields to photon annihilation in each resonator, $a_{1,(2),out} = \sqrt{\kappa_A}a - a_{2,(1),in} + \sqrt{\kappa_{Bx}}b$ and $b_{3,(4),out} = \sqrt{\kappa_B}b - b_{4,(3),in} + \sqrt{\kappa_{Ax}}a$, are used in the analysis [46]. We assume that only one input field $a_{1,in}$ (i.e., $a_{2,in} = b_{4,in} = b_{3,in} = 0$) is present for $S_{21}$ and $b_{3,in}$ (i.e., $a_{2,in} = b_{4,in} = a_{1,in} = 0$) for $S_{43}$. The details of this theoretical analysis are described in Appendix B.

We next confine ourselves to degenerate modes $\omega_A = \omega_B = \omega_r$ and, for simplicity, $m$-group TLSs (which belong to the capacitor pair associated with $M$ TLSs of group $m$). We can see from the Hamiltonian that for positive $\Omega_{AB}$, the $M$ TLSs are interacting with the lower-frequency mode. We also reduce the calculation to equal coupling and photon decay rates in each resonator, $\kappa_A = \kappa_B = \kappa_r, \gamma_A = \gamma_B = \gamma_r$, and assume that each resonator is decoupled from the other transmission line, $\kappa_{Ax} = \kappa_{Bx} = 0$. In the low-temperature and low-drive power limit ($k_B T \ll \hbar\omega$ and $n_{\rm ph} \ll 1$), the resonator will be asymptotically close to the ground state and we find the transmission amplitude of this four-port system to be given by

$$S_{43} = S_{21} = 1 - \kappa_r \frac{-i(\omega - \omega_r') + \kappa_r + \gamma_r}{-(\omega - \omega_r')^2 + (\kappa_r + \gamma_r)^2 - \left(i\Omega_{AB} - \sum_i^M \frac{\tanh(\frac{\hbar\omega}{2k_BT}) g_i^2}{-i(\omega - \omega_{\rm TLS}^i) + \frac{\gamma_{\rm TLS}^i}{2}}\right)^2 - 2i(\kappa_r + \gamma_r)(\omega - \omega_r')}, \tag{4}$$

where

$$\omega_r' = \omega_r - \sum_i^M \frac{\tanh(\frac{\hbar\omega}{2k_BT}) g_i^2}{\omega - \omega_{\rm TLS} + i\frac{\gamma_{\rm TLS}}{2}}.$$

For completeness, we provide in Appendix B the transmission for TLSs interacting with the high-frequency mode [Eq. (B15)] and that of the standard-coupled resonator pair [Eq. (B20)], as well as the cross-transmission from port 3 to port 2 ($S_{23}$), and from port 1 to port 4 ($S_{41}$), with nonzero $\kappa_{Ax}$ and $\kappa_{Bx}$ [Eqs. (B14) and (B15)].

### B. Theoretical results

In order to investigate the effect of TLS noise on the two resonator modes, we use the analytical results derived from Eq. (4) for both transmission lines in the limit of a weakly coupled TLS where $g \ll \Omega_{AB}$. The system that we consider is shown in Fig. 4(a). Figures 4(b) and 4(c) show the spectra of transmission $|S_{21}|$ for a TLS with the uncoupled modes in the standard-coupled design and the DuRKID, respectively. As shown, a given TLS in the DuRKID generally only shifts one of the two hybridized modes [see Fig. 4(c)], as expected. This is true even for a TLS that is detuned from the coupled modes (related to hybridized mode symmetries). In contrast, a TLS in either capacitor in the standard degenerate design will couple with equal strength to the two modes and cause a frequency shift to both [see Fig. 4(b)]. The difference is evident from the TLS-resonator interaction term in Eq. (1), which differs from the standard-coupled resonators (see Eq. (B20) in Appendix B). Thus the DuRKID has single-mode noise for a single TLS, whereas a standard-coupled TLS has correlated-mode noise (for more data on the off-resonance TLS case, see Appendix B). We also consider the case of a strong readout tone from port 1 or port 3 (see also Appendix A). In Fig. 4(d), the transmission spectra are shown in the presence of a strong pump drive with $H_d = i\hbar\sqrt{\kappa_A}A(t)a^\dagger$, where $\langle a_{1,\rm in}(t)\rangle = A(t)$ and $\langle a_{2,\rm in}(t)\rangle = \langle b_{3,\rm in}(t)\rangle = \langle b_{4,\rm in}(t)\rangle = 0$. As shown, a given TLS in the bridge-capacitor design, even in the presence of the strong pump drive, only shifts one of the two hybridized modes. Figure 4(e) shows the simulated signal on both resonance modes in the bridge-resonator design viewed from transmission spectra $1 \to 2$ (with $Z_A, Z_B \to 0$). Specifically, the solid line shows the transmission with a signal that increases $L_B$, as expected for a KID. We see, relative to the unperturbed transmission (dashed line), that the transmission spectra have a shift in both resonance modes to a lower frequency, as expected from earlier arguments. In addition, the relative sizes of the observed transmission notches are changed due to the way in which the modes are changed qualitatively—one mode is more $A$-like; the other mode is more $B$-like. In summary, one DuRKID mode will experience frequency shifts from one set of capacitors [$m$-group TLSs in Eq. (4)] that will shift a single mode; this is distinguishable from two correlated modes caused by the signal.

Figure 4(f) shows the transmission spectra of the DuRKID in the presence of two TLSs, one from each group (a capacitor pair). Next, this arrangement with two TLSs is used to calculate the cross-spectral density with TLSs and the two noise sources. For this, we simulate the TLS-induced frequency noise of two resonator modes split by $\Omega_{AB}$, with bare resonance frequencies of $\omega_0/2\pi = 3.533$ GHz. The frequency noise spectral density $S_{\delta\nu/\nu}(f)$ is simulated with one TLS from each TLS group ($m$ or $n$), by setting a $1/f$ noise spectrum on each.

In Fig. 5(a), we show the simulated frequency-noise spectral density for resonators $A$ and $B$. TLS frequency fluctuations in turn create fluctuations in the resonator modes, according to their effective couplings. The TLS with higher energy is coupled to the higher resonator mode, while the lower-energy TLS is coupled to the lower mode. These conditions create uncorrelated $1/f$ frequency noise in the resonator modes (see Appendix B). Im[$S_{21}$] versus Re[$S_{21}$] is shown in Figs. 5(b) and 5(c) without a TLSs coupled ($g = 0$, red line) and with two TLSs coupled (dark gray line). In this section, we are analyzing two

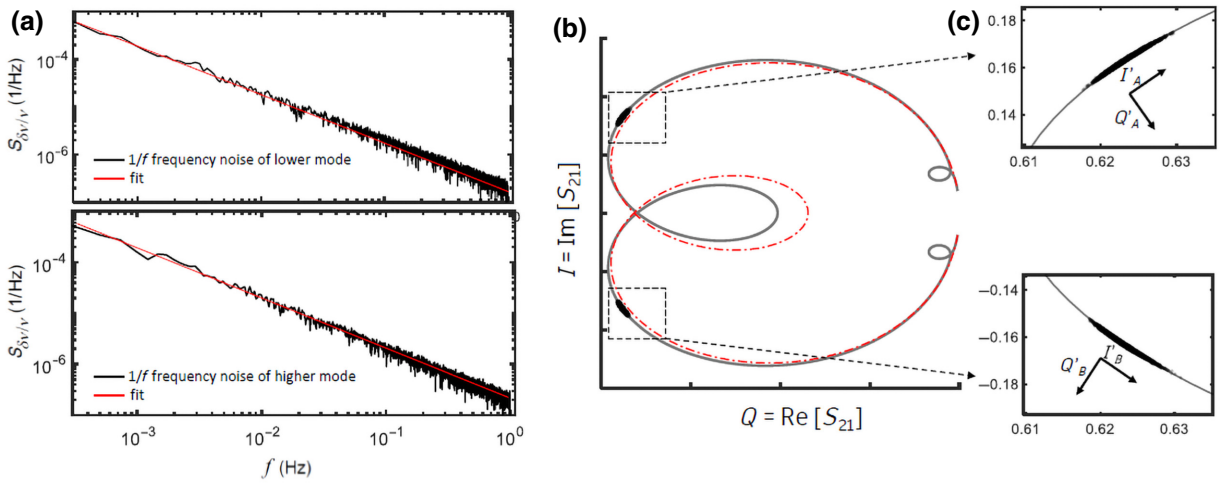


FIG. 5. The noise analysis for $1/f^{\alpha} \sim 1/f$ TLS noise, using time-domain simulations for two variable-frequency TLSs. (a) The fractional-frequency noise spectral density $S_{\delta\nu/\nu}$ for the two resonator modes. The solid line is fitted to $A/[f/(1\,\mathrm{Hz})] + B$, where we define $A$ as the $1/f$ noise density and $B$ as the white-noise density. (b) The complex transmission, $\mathrm{Im}[S_{21}]$ versus $\mathrm{Re}[S_{21}]$, for the DuRKID with two TLSs (black line), where there is one TLS from the $m$ and $n$ groups, which, according to the design, implies that each TLS couples to only one mode. The red dashed line is shown for the transmission without TLSs (this has been numerically obtained with zero TLS coupling, which is equivalent). The black solid and red dashed lines can be compared to the transmission magnitude versus the frequency [see Fig. 4(f)], where there are four minima in the case of coupled TLSs, and where two large minima show the DuRKID resonances. Accumulated points from the transmission time-domain simulation at two fixed input frequencies are shown as black points in two dashed boxes. The two sets of accumulated points are further apart in $I = \mathrm{Im}[S_{21}]$ than naively expected from the $Q = \mathrm{Re}[S_{21}]$ minima on the transmission curve. This is because the input frequencies for TLS noise analysis are chosen at the resonance frequencies without coupled TLS, which have increased difference in frequency as well as increased difference in $I = \mathrm{Im}[S_{2,1}]$ relative to the case with coupled TLSs. (c) An enlarged view of the transmission points accumulated in time for fixed input frequencies (black points). The transmission for various frequencies is shown as a gray line. Upper panel: the $I'_A$ quadrature is defined as the tangent of the transmission versus the frequency on the first mode. Lower panel: the $I'_B$ quadrature is defined as the tangent of the transmission versus the frequency on the second mode. The TLS noise in the resonator modes is uncorrelated due to separated noise sources, unlike the single-mode frequency-quadrature signal from a standard KID.

TLSs from two separate capacitor groups. The noise is further modeled in Sec. IV using external noise sources that will be present in a system, and the addition of internal noise from stray capacitance.

## IV. SYSTEM-NOISE ANALYSIS

Next, we compare the expected noise from the DuRKID readout with that of a standard KID. In our earlier discussion, we have mainly analyzed the TLS noise in terms of frequency change (and frequency quadrature in transmission). However, a standard KID partially mitigates TLS noise by also measuring the dissipation quadrature. Thus, this analysis is important for a fair comparison.

Our model starts by specifying a dissipation-to-frequency responsivity (a responsivity ratio) from quasiparticles created in the illuminated inductor. Figure 6 shows this responsivity ratio calculated from the Mattis-Bardeen formula as a function of the operating temperature relative to the superconducting transition temperature and of the resonance frequency relative to the superconducting gap frequency. For some applications, e.g., NASA's EXCLAIM mission [47], the reduced temperature and frequency operating point corresponds to a relatively large responsivity ratio and a single-mode KID can mitigate TLS noise fairly well. The implementation uses thin-film aluminum MKIDs operating at 168 mK and 3.5 GHz. Furthermore, in the EXCLAIM mission, $(T/T_c, f/f_{\mathrm{gap}}) =$

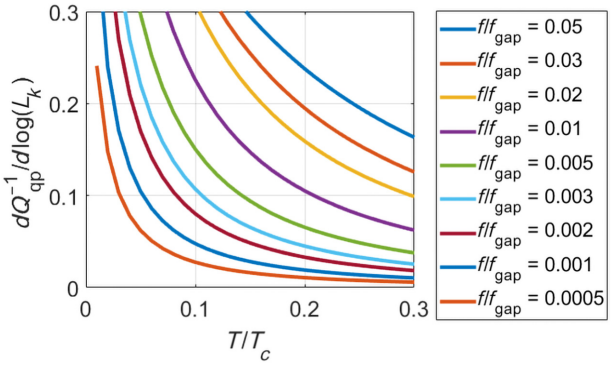


FIG. 6. The responsivity ratio between the dissipation and frequency readout channels for a KID, as a function of the reduced operating temperature and readout frequency. The noise analysis in this section is calculated using a responsivity ratio of 0.03.

$(0.13, 0.035)$, which results in a responsivity ratio of $dQ_{\rm qp}^{-1}/d\log(L_k) \approx 0.3$ in the KID. Here, $\log(L_k)$ is the natural logarithm of the kinetic inductance and $Q_{\rm qp}$ is the internal quality factor from quasiparticles. For other circumstances, one may employ larger capacitors and also a lower resonance frequency, such as a thin aluminum resonator operating at 200 mK and 0.5 GHz, which has $(T/T_c, f/f_{\rm gap}) = (0.15, 0.005)$, giving a responsivity ratio of approximately 0.095. In our noise analysis, we have chosen the responsivity ratio of 0.03 as a realistic experimental condition that creates $1/f$ -noise limitations.

Similar to previous studies [48–50], our noise model describes the noise-equivalent power (NEP). Besides TLS-induced $1/f$ noise, the model includes generation-recombination (G-R) noise from quasiparticle fluctuations in the superconducting inductors [51] and readout-amplifier noise. The signal frequency response of the detector is assumed to roll off with a time constant equal to the quasiparticle lifetime $\tau_{\rm qp}$. Capacitance fluctuations are used to describe TLS induced $1/f$ noise in this model; these fluctuations are created by the TLS noise and they also provide sufficient detail for the purpose at hand. For the DuRKID, we have used a circuit model to evaluate the responsivity of the in-phase (real part) and quadrature (imaginary part) of $S_{43}$ to changes in each capacitor in the circuit, as well as to changes in the inductance and dissipation (in accordance with the responsivity ratio) from illumination.

The model of the DuRKID for the noise analysis of this section is shown in Fig. 7(a). For a realistic model, we have added capacitance $C_5$, which was not shown earlier, in Fig. 1(b). This represents the stray capacitance in our circuit, as it is not present in an ideal capacitance bridge. TLSs in this capacitance will appear on the resonance mode $B$ (before hybridization) such that $C_5$ introduces noise on both modes when hybridized: nominally the ($C_1$, $C_3$) mode and the ($C_2$, $C_4$) mode are affected when the detector is perturbed by $C_5$. The stray-capacitance and relative-capacitance changes from the TLS in the analysis are estimated from the fabricated circuit geometry shown in Fig. 2(a).

To compute the NEP, we have used the method in Sec. IIB of Ref. [52], which describes the theory of optimal linear filtering to maximize the signal-to-noise ratio for a detector with a vector output $\mathbf{x}$. In the case of a DuRKID, the detector system has a four-component vector output comprised of, e.g., the real and imaginary parts of $S_{43}$ probed at the two microwave resonance frequencies [similar to the transmission shown in Fig. 5(c)]. The first step of the NEP calculation involves evaluating the cross-spectral density matrix $\mathbf{S_x}$ between the components of the signal vector $\mathbf{x}$ using the assumed noise sources and the responsivity of the signal to changes in circuit parameters. One such responsivity matrix, $\mathbf{M}$, is shown in Fig. 7(b), where the first row represents the components from an

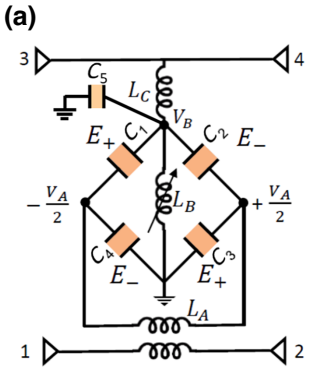


| | $dI_{\omega_1}$ | $dQ_{\omega_1}$ | $dI_{\omega_2}$ | $dQ_{\omega_2}$ |
|---|---|---|---|---|
| $d\ln L_B$ | 34.70 | 85.27 | 72.09 | 25.08 |
| $d\ln C_1$ | −6.435 | −2.117 | 40.50 | 50.48 |
| $d\ln C_2$ | 59.16 | 52.13 | −0.6525 | −5.383 |
| $d\ln C_3$ | −6.412 | −2.157 | 40.47 | 50.49 |
| $d\ln C_4$ | 59.18 | 52.09 | −0.6871 | −5.369 |
| $d\ln C_5$ | 0.3387 | 0.9958 | 0.8137 | 0.3315 |

FIG. 7. (a) The circuit schematic for DuRKID. This schematic includes stray capacitance $C_5$, which is outside of the intended capacitive electrical bridge. (b) The responsivity matrix $\mathbf{M}$. This is the derivative of the vector composed of the four DuRKID measurement channels ($I$-$Q$ components of $S_{43}$ at the two resonance frequencies) with respect to the fractional change of six detector parameters. The detector parameters with fluctuations are the inductance $L_B$ (with a dissipative response direction dictated by the responsivity ratio) and five capacitances $C_1$–$C_5$ (related to TLS-induced noise). The size of the changes is modeled using the device parameters, including the measured quality factors.

illumination signal, which we describe, for brevity, as being optical. In the remaining five rows, we represent the components from the TLS-induced capacitance noise. The cross-spectral density matrix is $\mathbf{S_x} = \mathbf{M^T D M} + \mathbf{S_{x0}}$, where $\mathbf{D}(\omega)$ is a diagonal matrix with the spectral density for fluctuations in each of the six internal circuit parameters and $\mathbf{S_{x0}}$ is the white noise from the microwave readout amplifier.

The remaining steps in the NEP calculation are as follows: (i) compute the inverse of the cross-spectral density matrix $\mathbf{S_x^{-1}}$, (ii) compute the vector signal expected from a unit impulsive change in the optical power $\mathbf{x}_{\rm sig}(\omega)$, (iii) compute the signal-to-noise ratio spectral density $\sigma(\omega) = \mathbf{x}_{\rm sig}^{\dagger}\mathbf{S_x^{-1}}\mathbf{x}_{\rm sig}$, and finally (iv) obtain the NEP from the square root of the reciprocal of the signal-to-noise ratio spectral density.

Figure 8 shows the resulting NEP versus signal frequency for four example cases: (i) DuRKID readout using two-probe tones to monitor both modes of the dual resonator, (ii) DuRKID readout using only a single probe tone, (iii) single-mode KID readout using both its frequency and dissipation response channels, and (iv) single-mode KID readout using only its frequency channel. As discussed above, we have chose to model the case of a dissipation-to-frequency responsivity ratio of 0.03. This illustrative example analysis uses a ratio of HEMT white-noise power to generation-recombination (G-R) noise power at zero frequency of 0.2, a ratio of TLS noise power at $\omega_{\rm QP} = 1/\tau_{\rm qp}$ to G-R noise power at zero frequency of 0.5, and a ratio of TLS fractional capacitance noise in $C_5$ at

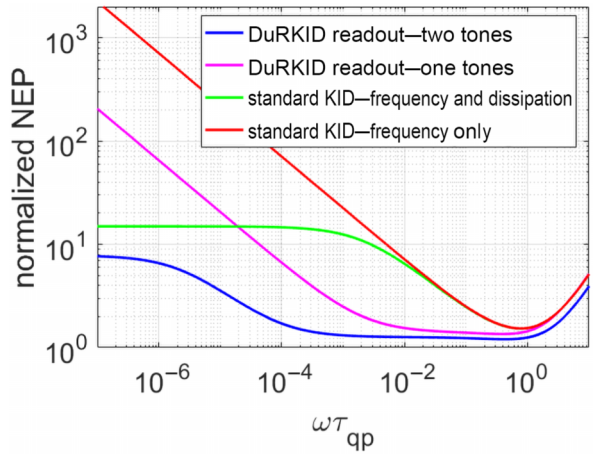


FIG. 8. The noise-equivalent power (NEP) relative to the generation-recombination (G-R) noise level for four cases: a two-tone DuRKID readout (as intended), a single-tone DuRKID readout, and a standard KID readout with the frequency quadrature readout, and a KID readout using both the frequency and dissipation quadrature (see the text for parameters). The horizontal axis shows the signal frequency multiplied by the quasiparticle lifetime $\tau_{qp}$. Note that the DuRKID read out with two tones (blue trace) performs substantially better in this case than the standard KID with two quadratures (green line), over a range of frequencies below the inverse quasiparticle lifetime.

2 times larger than that in the designed capacitors ($C_1$–$C_4$). Additionally, the frequency dependence of the TLS noise is taken to be an ideal $1/f$ exponent. The NEP shown in the figure is normalized to (divided by) the G-R noise at zero frequency.

The single-tone readout of the DuRKID shows the NEP degrading without limit as the signal frequency approaches zero (purple line). This limiting behavior occurs because when only two components (i.e., the in-phase and quadrature ($I$-$Q$) response from the single probe tone) are measured, there exists a linear combination of TLS capacitance fluctuations in $C_5$, $C_2$ (or $C_4$), and $C_1$ (or $C_3$) that looks similar to a response from quasiparticle generation caused by weak optical illumination of the inductor (with fractional inductance change accompanied by the assumed 3% smaller change in $1/Q$ due to quasiparticle dissipation). In contrast, when four components are measured (i.e., the $I$ and $Q$ components from $f_-$ and $f_+$), then the signal vector for a quasiparticle response to inductor illumination is not contained within the vector space of outputs in response to all possible changes in $C_5$, $C_2$ (or $C_4$), and $C_1$ (or $C_3$). In other words, if only a single-tone readout is used from the double resonator DuRKID circuit, then there is not enough information measured to distinguish an optical response from some possible combinations of TLS fluctuations in the various capacitors in the circuit. Also, we find that $C_5$ TLS fluctuations are not needed to spoil the single-tone readout of a DuRKID. Symmetry breaking in the circuit with a single-tone readout can give a nonzero response at $f_-$ to $C_1$ and $C_3$ fluctuations and $f_+$ to $C_2$ and $C_4$ fluctuations, which can also spoil the information of a DuRKID and its related ability to overcome TLS noise.

However, when a two-tone readout is used in a DURKID (blue line), one can best distinguish an optical response from any possible TLS fluctuation. This contrasts with a standard single-resonator KID, where a single-tone $I$-$Q$ readout does suffice to give an optical-response-signal vector that is outside the (one-dimensional) vector space of fluctuations in the readout. In a standard KID detector, the frequency-only quadrature measurement is generally worse (red line) than the one-tone DuRKID readout (purple line) due to less information about the signal, resulting in higher $1/f$ noise. In fact, the one-tone DURKID readout has an advantage in this comparison for frequencies $\omega\tau_{qp} < 10^{-1}$, because the DuRKID distinguishes signal from $1/f$ noise due to new information of the signal relative to capacitance noise in this frequency regime. When the dissipation quadrature is added to the standard KID readout (green line), TLS noise is partially avoided and it performs within a factor of 2 of the intended DuRKID in NEP at the lowest frequencies. The most striking regime for improvement for the DuRKID is an intermediate frequency range from $10^{-5} < \omega\tau_{qp} < 10^{-1}$. This behavior is related to the low influence from noise in $C_5$ from the DuRKID (blue line) relative to a standard KID, which can only mitigate $1/f$ noise above some noise level (green line). In an intermediate frequency regime, which of course depends on the model parameters, one can expect the DuRKID to perform as an improved alternative to the standard KID.

### A. System-noise discussion

The NEP generally depends on the optical (absorber) power [53] and the readout power. Empirically, TLS-induced phase noise is proportional to the inverse root of the measurement power [3]. However, the generation-recombination noise will also increase with the optical power. To allow a close comparison between a standard KID and a DuRKID, the DuRKID could be read out at approximately twice the total readout power relative to a standard KID such that the stored energy per inductor is equal in the KIDs. Furthermore, the reference KID should also use the same capacitor volume as the DuRKID. In this case, there will be a $\sqrt{2}$ decrease in the rms voltage in the DURKID relative to the KID. This will slightly increase the TLS $1/f$ noise for one measurement channel of the DuRKID relative to the KID. However, there is a potential order-of-magnitude decrease in NEP in the DuRKID. While the DuRKID performance can be substantially better than that of the standard KID, the TLS noise difference is not precisely known, because there can be some decrease in noise from saturation of the TLSs by the adjacent readout tone.

Due to the power dependences of NEP, the DuRKID seems most likely to make an impact on low-illumination-power IR KIDs. One such KID is a mid-IR KID designed for NASA's GEP mission [53]. Another example is an IR KID detector that might be designed to reach the power sensitivity permitted by the Origins Space Telescope (OST), $10^{-20}$ W/$\sqrt{\text{Hz}}$ [54].

The generation-recombination noise in the inductor of a KID relates to the breaking of Cooper pairs, which is a quasiparticle noise term [55]. Quasiparticle noise is quantitatively different in QIP hardware than KID hardware for two reasons. First, substantial kinetic inductance is rarely used in film-based inductors in QIP because there is a desire to remove all quasiparticles, since they will induce loss in accord with the two-fluid model and result in quantum information loss via relaxation. Secondly, a low-density of quasiparticles is needed for stable frequencies in qubits and resonators of QIPs, while high kinetic inductance in films [56] is required for a substantial illumination response in KIDs, despite the significant level of quasiparticle generation-recombination noise.

## V. CONCLUSIONS

We have proposed a new KID detector design named DuRKID, which includes an electrical bridge and two resonance modes. The DuRKID has been fabricated with two feed lines, where each is primarily coupled to one of the resonance modes when the modes are not hybridized. Measurements of the fabricated device have revealed that the frequency tuning of one mode allows the hybridization of the modes, as required for the intended operation. In the DuRKID, the TLS noise in the two modes is caused by different TLSs and capacitors such that the noise from the groups of TLSs is qualitatively different.

From transmission measurements on the DuRKID, we have found that the coupling between the modes is larger than the coupling of a TLS to a resonator mode. Furthermore, to achieve degeneracy we have merely needed to tune a resonator with an applied dc-bias current, where the largest tuning is approximately 120 MHz. To show that a specific TLS is coupled to only one of the fully hybridized modes, we have applied the input-output theory, a formalism from quantum information science, to analyze the DuRKID. This model has included four ports coupled to two resonators, with one representative TLS of each capacitor group in the bridge, and has allowed a model of TLS noise in the DuRKID. The model also allowed us to extract the capacitor loss tangents, inter-resonator coupling, and the intended and unintended couplings to transmission lines from data.

From our model of $1/f$ noise in the DURKID, we have found that the TLS noise gives a lack of correlation in the two hybridized modes over time, as expected. This represents a potentially useful capability in a KID-type detector. Additionally, we have also modeled the system NEP of our DuRKID with a comparison to a standard KID using the expected noise sources and all of the possible readout channels. The DuRKID generally gives additional information, and thus lower NEP, relative to a standard KID. Moreover, the analysis shows that there can be a multidecade-wide frequency band that exhibits noise that is over an order of magnitude lower for a DuRKID relative to a standard KID. In the future, we plan to measure the NEP of a DuRKID as a function of the frequency.

## ACKNOWLEDGMENTS

We thank F. C. Wellstood, C. Richardson, R. Ruskov, and W. Wustmann for scientific discussions. This work was partially funded through a NASA Science Innovation Fund (SIF) award. B.S. acknowledges funding through the Intelligence Community Postdoctoral Research Fellowship Program.

## APPENDIX A: NONLINEARITY OF THE KINETIC INDUCTANCE AND THE FITTING PROCEDURE

### 1. Nonlinearity of the kinetic inductance

As described in the main text, the inductance of the $LC$ resonators is made tunable with dc bias. We have measured the nonlinearity explicitly in device 2 at millikelvin temperature with a direct applied bias current (note that devices 1 and 3 share a single dc-input current in parallel). The relationship has previously been given for inductance as a quadratic function of the bias current but here we describe the nonlinear inductance. The width of the TiN inductor is 5 mm. Figure 9(a) shows the frequency of the resonator as a function of the square of the bias current. The fractional resonance frequency shift can be written in terms of the current or the inductance as

$$\frac{\delta f_r}{f_r} = -\frac{I_b^2}{2I'^2} = -\frac{\delta L_r}{2L_r}. \tag{A1}$$

We have fitted to a quadratic model as a function of the bias current $I_b$ as shown in Fig. 9(a) and from this we have extracted $I' = 789$ μA. In Fig. 9(b), we show the same type of fit, except that we use the inductance as the independent variable rather than the frequency.

### 2. The fitting procedure

In order to fit the measured complex transmission data, $S_{21}$, $S_{43}$, and $S_{31}$, we use Eqs. (B14), (B15), and (B16). Although general formulas can be made to fit directly for the many parameters simultaneously, such multiparameter fitting problems can be extremely sensitive to the initial values, due to the local optimization of the parameters and different amounts of noise in different data sets. Fitting a

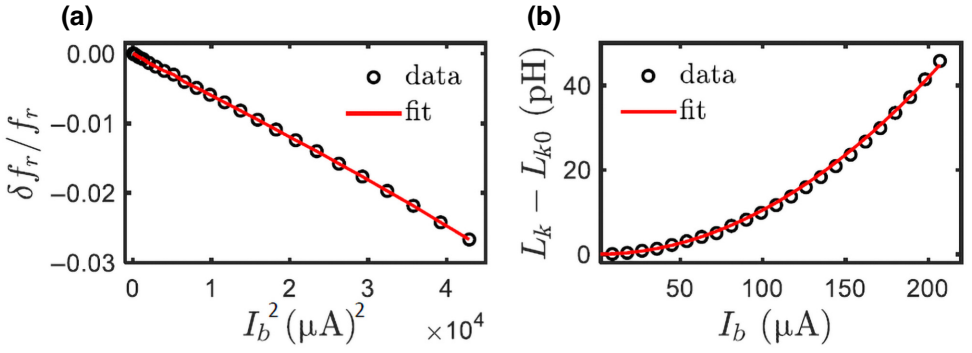


FIG. 9. The dependence of the (a) frequency and (b) kinetic inductance on $I_b$.

small subset of the data leads to under-determined constraints and inaccuracies due to covariances. To resolve this issue, we utilize an iterative procedure through which our fitting problem, with ten parameters, is broken down into several independent fitting problems with carefully chosen fixed parameters. Each fit contains only a few (two or three) parameters at a time. First, we extract the cross-coupling $\Omega_{AB}$ from the data of Fig. 3(c). We have previously performed resonator fittings from transmission data (e.g., $S_{21}$) using the diameter-correction method (DCM) (for a single resonator) [57]. This technique uses a least-squares Monte Carlo (LSM) method to find the minimum error, $\chi^2$. To fit both $S_{21}$ and $S_{43}$, we have developed a fitting sequence using a sequence of different LSM fittings in a multistep procedure. We start by using LSM fitting primarily with $S_{21}$ data, using the device model given in Eq. (B14), except that an extra multiplicative factor $e^{i\theta}$ is applied to the right-hand side of Eq. (B14) to account for the transmission-line length. Initial guesses must be placed for all variables, including $\omega_A$, $\omega_B$, $\kappa_A$, $\kappa_B$, $\gamma_A$, $\gamma_B$, $\kappa_{Ax}$, and $\kappa_{Bx}$ . Within the LSM fitting, a Monte Carlo guess is made in the form $x = x_0 e^{\zeta\xi}$ for each fit parameter, where $x_0$ is the previous (initial) guess for the fit parameter $x$, $\zeta$ is a randomly generated number between $-1$ and 1, and $\xi$ is a parameter smaller than one, which determines the MC guess domain.

However, to optimize $S_{21}$ in the first fit, we use two different values of $\xi$ for the different parameters. For parameters associated with resonator $B$, we use fast iterations, e.g., we use $\xi = 0.1$ for $\omega_A$, $\kappa_A$, $\gamma_A$, $\kappa_{Ax}$, and $\theta_{21}$ to optimize it quickly. Meanwhile, for parameters associated with resonator $A$, we use slow iterations, e.g., we use $\xi = 10^{-5}$ for $\omega_B$, $\kappa_B$, $\gamma_B$, $\kappa_{Bx}$, and $\theta_{43}$, to leave the parameters with only slight changes. After this step, the updated values are used to fit $S_{43}$ following the same procedure, with the difference that this time the variation of the resonator-$A$ parameters is quickly optimized and the resonator-$B$ parameters are mainly left unchanged. Next, the $S_{43}$ fit parameters are determined, such that $S_{21}$ could be fitted, and this completes one cycle of our procedure. The previous two steps are repeated in sequence: e.g., by using the fitting results from $S_{21}$ ($S_{43}$), we then fit $S_{43}$ ($S_{21}$). The fitting cycles are then repeated iteratively many times until convergence is obtained. The standard resonator coupling to the intended transmission line is $Q_c^{A,B} = \omega_{A,B}/2\kappa_{A,B}$. The internal loss from one resonator is often desired, which is $Q_i = \omega/\gamma$ in our devices, where the resonator loss $1/Q_i$ is due to the sole dielectric in each resonator. Since we have a dual-transmission-line setup, it is useful to define the apparent internal quality factor for each resonator, $Q_{i,\mathrm{app}}^{A,B} = \omega_{A,B}/(\gamma_{A,B} + 2\kappa_{Ax,Bx})$, which not only depends on the internal loss rate of the resonator to its internal loss $\gamma_{a,b}$ but also the coupling loss to the unintended transmission line $2\kappa_{Ax,Bx}$, respectively. Figures 7(a) and 7(b) show an example of such a fit to two resonance line shapes for resonators $A$ and $B$, which are coupled to transmission lines 1–2 and 3–4, respectively, for $-140$ dB power at the device. The extracted fitting parameters from $S_{21}$ and $S_{43}$ are used as initial guesses to fit the cross transmission from port 1 to port 4, $S_{41}$.

## APPENDIX B: DERIVATION OF THE TRANSMISSION FOR TWO RESONANCES INTERACTING WITH TLS

### 1. *LC* resonator pair with an internal electrical bridge of capacitors

The system that we consider in Fig. 1(a) consists of two resonators and TLSs, described by the Hamiltonian $H_{\mathrm{sys}}$ [Eq. (2)]. It is coupled to two transmission lines that are accessible at their ends via four ports. The system has resonator modes $a$ and $b$. According to the standard theory of input and output for quantum dissipative systems [41], the transmission lines can be modeled as a heat bath. Additionally, the couplings can be specified between transmission lines and the intended couplings, $\kappa_A$ and $\kappa_B$, as well as the unintended couplings, $\kappa_{Ax}$ and $\kappa_{Bx}$. The Heisenberg equation of motion for the bare-resonator modes in terms of the system and output fields [c.f. Eqs. (2) and (3)] can be written as

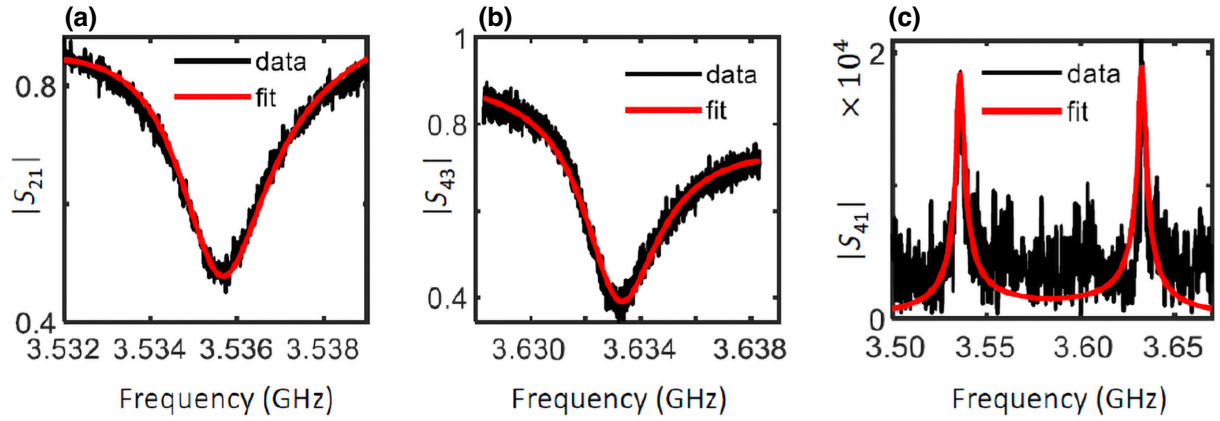


FIG. 10. The transmission data in the absence of bias for (a) resonator $A$ and (b) resonator $B$. The red curves show the fit of the data to the model. The fit yields $\omega_A = 3.5357$ GHz, $\gamma_A = 0.88$ MHz, $\kappa_A = 0.9$ MHz, $\kappa_{Ax} = 20$ kHz, and $\omega_B = 3.6335$ GHz, $\gamma_B = 0.77$ MHz, $\kappa_B = 1.01$ MHz, $\kappa_{Bx} = 19.7$ kHz, $Q_i^A = 2741$, $Q_i^B = 3026$ and $Q_c^A = 1930$, $Q_c^B = 1800$. (c) The crosstalk coupling (unintended coupling) between ports 1 and 4 of device 2 in the absence of bias. The fitting data give 20.3 kHz of cross-coupling between ports 1 and 4, with $\omega_A = 3.534$ GHz, $\gamma_A = 0.91$ MHz, $\kappa_A = 0.97$ MHz, $\kappa_{Ax} = 20.3$ kHz, and $\omega_B = 3.6335$ GHz, $\gamma_B = 0.77$ MHz, $\kappa_B = 1.01$ MHz, $\kappa_{Bx} = 19.5$ kHz. The agreement between the data and four-port model confirms the appropriateness of the fitting method and the many parameter models.

$$\frac{d}{dt}\langle a\rangle = -i\omega\langle a\rangle = -\frac{i}{\hbar}\langle[a, H_{\rm sys}]\rangle + \kappa_A\langle a\rangle - \sqrt{\kappa_A}\langle a_{1,\rm out}\rangle - \sqrt{\kappa_A}\langle a_{2,\rm out}\rangle$$
$$- \sqrt{\kappa_{Ax}}\langle b_{3,\rm out}\rangle - \sqrt{\kappa_{Ax}}\langle b_{4,\rm out}\rangle - \gamma_A\langle a\rangle + \kappa_{Ax}\langle a\rangle + \sqrt{\kappa_A\kappa_{Bx}}\langle b\rangle + \sqrt{\kappa_{Ax}\kappa_B}\langle b\rangle \tag{B1}$$

and

$$\frac{d}{dt}\langle b\rangle = -i\omega\langle b\rangle = -\frac{i}{\hbar}\langle[b, H_{\rm sys}]\rangle + \kappa_B\langle b\rangle - \sqrt{\kappa_B}\langle b_{3,\rm out}\rangle - \sqrt{\kappa_B}\langle b_{4,\rm out}\rangle$$
$$- \sqrt{\kappa_{Bx}}\langle a_{1,\rm out}\rangle - \sqrt{\kappa_{Bx}}\langle a_{2,\rm out}\rangle - \gamma_B\langle b\rangle + \kappa_{Bx}\langle b\rangle + \sqrt{\kappa_B\kappa_{Ax}}\langle a\rangle + \sqrt{\kappa_{Bx}\kappa_A}\langle a\rangle\,. \tag{B2}$$

We write the equation of motion for the operator $\sigma_i^-$ of the $i$th TLS using the Bloch equations approximation for relaxation and decoherence,

$$\frac{d}{dt}\langle\sigma_i^-\rangle = -i\omega\langle\sigma_i^-\rangle = -i\omega_{{\rm TLS},i}\langle\sigma_i^-\rangle - \frac{\gamma_{{\rm TLS},i}}{2}\langle\sigma_i^-\rangle + 2g\langle\sigma_i^z a\rangle + 2g\langle\sigma_i^z b\rangle\,, \tag{B3}$$

where the TLS decoherence rate is $\gamma_{{\rm TLS},i} = k_{1,i} + 2k_{2,i}$, in which typically $k_{1,i} = A_1\Delta_{0,i}^2{\rm coth}\,(\hbar\omega/2k_BT)$ and $k_{2,i} \approx A_2{\rm T}^2$. The rates $k_{1,i}$ and $k_{2,i}$ describe the TLS $i$ relaxation and phase decoherence rates associated with TLS-photon and TLS-TLS interactions, respectively, and $A_1$ and $A_2$ are material-related constants [58]. In the low-temperature and low-drive-power limit ($k_BT \ll \hbar\omega$ and $n_{\rm ph} \ll 1$), the resonator will be asymptotically close to the ground state. This suggests that we can replace the spin operator $\langle\sigma_i^z\rangle$ in Eq. (B3) with the ground-state value $-1/2$. With these assumptions, we obtain a closed system of linear equations that can be solved for the TLS operators:

$$\langle\sigma_i^-\rangle = \frac{2g(\langle a\rangle + \langle b\rangle)\langle\sigma_i^z\rangle}{i(\omega_{{\rm TLS},i} - \omega) + \frac{\gamma_{{\rm TLS},i}}{2}}. \tag{B4}$$

For thermally excited TLSs, one can use a mean-field approach, replacing the operator $\langle\sigma_i^z\rangle$ in Eq. (B3) with its thermodynamic average value, i.e., $\langle\sigma_{i\,\rm th}^z\rangle = -1/(2)\tanh(\hbar\omega/2k_BT)$. This approach is consistent with previous analysis of sound and microwave absorption by TLSs [59,60]. The average value of $\langle\sigma_i^z\rangle$ at a higher photon regime is calculated in Sec. B 3.

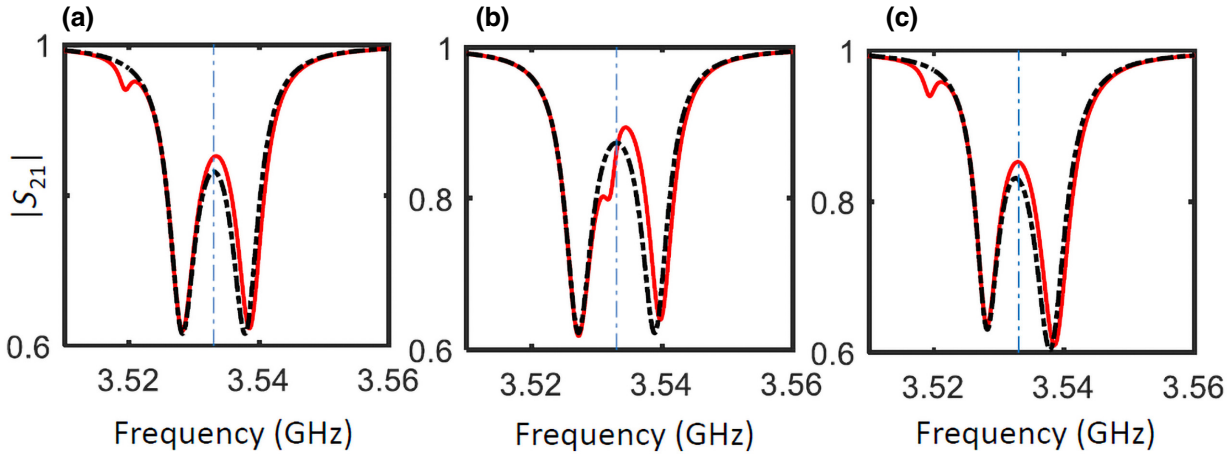


FIG. 11. (a) The simulated transmission magnitude $|S_{21}|$ (with $Z_B \to 0$ ) for a single TLS off resonance coupled to the $a+b$ field in the bridge design. The TLS frequency of $\omega_{\rm tls} = 3.52$ GHz is used here and the rest of the parameters are the same as before. Note that dispersion is not caused at the neighboring frequency mode but at the mode that has the proper coupling for the TLSs capacitor. (b) The impact of a single TLS on resonance coupled to the $a+b$ field on both hybridized modes. (c) The impact of nonzero unintended coupling of each resonator to the other transmission line, $\kappa_{Ax} = \kappa_{Bx} = 20$ kHz for the data presented in (a).

To proceed, we now substitute the solution for $\langle \sigma_i^- \rangle$ [Eq. (B4)] into Eqs. (2)–(4) and obtain the solution for resonator modes $a$ and $b$:

$$L_{A,+}\langle a\rangle + L_{AB,+}\langle b\rangle = \sqrt{\kappa_A}\langle a_{1,\rm in}\rangle + \sqrt{\kappa_A}\langle a_{2,\rm in}\rangle + \sqrt{\kappa_{Ax}}\langle b_{3,\rm in}\rangle + \sqrt{\kappa_{Ax}}\langle b_{4,\rm in}\rangle, \tag{B5}$$

$$L_{A,-}\langle a\rangle + L_{AB,-}\langle b\rangle = -\sqrt{\kappa_A}\langle a_{1,\rm out}\rangle - \sqrt{\kappa_A}\langle a_{2,\rm out}\rangle - \sqrt{\kappa_{Ax}}\langle b_{3,\rm out}\rangle - \sqrt{\kappa_{Ax}}\langle b_{4,\rm out}\rangle, \tag{B6}$$

$$L_{B,+}\langle b\rangle + L_{AB,+}\langle a\rangle = \sqrt{\kappa_B}\langle b_{3,\rm in}\rangle + \sqrt{\kappa_B}\langle b_{4,\rm in}\rangle + \sqrt{\kappa_{Bx}}\langle a_{1,\rm in}\rangle + \sqrt{\kappa_{Bx}}\langle a_{2,\rm in}\rangle, \tag{B7}$$

$$L_{B,-}\langle b\rangle + L_{AB,-}\langle a\rangle = -\sqrt{\kappa_B}\langle b_{3,\rm out}\rangle - \sqrt{\kappa_B}\langle b_{4,\rm out}\rangle - \sqrt{\kappa_{Bx}}\langle a_{1,\rm out}\rangle - \sqrt{\kappa_{Bx}}\langle a_{2,\rm out}\rangle, \tag{B8}$$

where

$$L_{A,\pm} = -i\omega + i\omega_A + \gamma_A \pm \kappa_A \pm \kappa_{Ax} - \sum_{i=1}^{N} \frac{2sg_i^2}{i(\omega_{{\rm TLS},i} - \omega) + \frac{\gamma_{{\rm TLS},i}}{2}}, \tag{B9}$$

$$L_{AB,\pm} = i\Omega_{AB} \pm \sqrt{\kappa_A\kappa_{Bx}} \pm \sqrt{\kappa_{Ax}\kappa_B} - \sum_{i=1}^{N} \frac{2sg_i^2}{i(\omega_{{\rm TLS},i} - \omega) + \frac{\gamma_{{\rm TLS},i}}{2}}, \tag{B10}$$

$$L_{B,\pm} = -i\omega + i\omega_B + \gamma_B \pm \kappa_B \pm \kappa_{Bx} - \sum_{i=1}^{N} \frac{2sg_i^2}{i(\omega_{{\rm TLS},i} - \omega) + \frac{\gamma_{{\rm TLS},i}}{2}}. \tag{B11}$$

To study one coherent input, we then set $\langle a_{2,\rm in}\rangle = \langle b_{4,\rm in}\rangle = \langle b_{3,\rm in}\rangle = 0$ to calculate $S_{21}$ and $\langle a_{2,\rm in}\rangle = \langle b_{4,\rm in}\rangle = \langle a_{1,\rm in}\rangle = 0$ to calculate $S_{43}$. The solution for resonator modes $a$ and $b$ takes the form

$$\langle a\rangle = \frac{\sqrt{\kappa_A} - \frac{L_{AB,+}\sqrt{\kappa_{Bx}}}{L_{B,+}}}{L_{A,+} - \frac{L_{AB,+}^2}{L_{B,+}}}\langle a_{1,\rm in}\rangle \tag{B12}$$

and

$$\langle b\rangle = \frac{\sqrt{\kappa_{Bx}}}{L_{B,+}}\langle a_{1,\rm in}\rangle - \frac{L_{AB,+}}{L_{B,+}}\frac{\sqrt{\kappa_A} - \frac{L_{AB,+}\sqrt{\kappa_{Bx}}}{L_{B,+}}}{L_{A,+} - \frac{L_{AB,+}^2}{L_{B,+}}}\langle a_{1,\rm in}\rangle. \tag{B13}$$

Using the boundary conditions, $a_{1,(2),\mathrm{out}} = \sqrt{\kappa_A}a - a_{2,(1),\mathrm{in}} + \sqrt{\kappa_{Bx}}b$ and $b_{3,(4),\mathrm{out}} = \sqrt{\kappa_B}b - b_{4,(3),\mathrm{in}} + \sqrt{\kappa_{Ax}}a$, and Eqs. (B10) and (B11), we obtain $S_{21} = \langle a_{2,\mathrm{out}}\rangle/\langle a_{1,\mathrm{in}}\rangle$, $S_{43} = \langle b_{4,\mathrm{out}}\rangle/\langle b_{3,\mathrm{in}}\rangle$, and $S_{41} = \langle b_{4,\mathrm{out}}\rangle/\langle a_{1,\mathrm{in}}\rangle$ as

$$S_{21} = 1 - \frac{\kappa_A}{-i(\omega-\omega_A) + \kappa_A + \gamma_A - \sum_{i=1}^{N} \frac{2Sg_i^2}{-i\left(\omega-\omega_{\mathrm{TLS}}^i\right)+\frac{\gamma_{\mathrm{TLS}}^i}{2}} - \frac{\left(i\Omega_{AB} - \sum_{i=1}^{N}\left(\frac{2g_i^2}{-i\left(\omega-\omega_{\mathrm{TLS}}^i\right)+\frac{\gamma_{\mathrm{TLS}}^i}{2}}\right)\right)^2}{-i(\omega-\omega_B)+\kappa_B+\gamma_B-\sum_{i=1}^{N}\frac{2Sg_i^2}{-i\left(\omega-\omega_{\mathrm{TLS}}^i\right)+\frac{\gamma_{\mathrm{TLS}}^i}{2}}}}, \tag{B14}$$

$$S_{43} = 1 - \frac{\kappa_B}{-i(\omega-\omega_B) + \kappa_B + \gamma_B - \sum_{i=1}^{N} \frac{2Sg_i^2}{-i\left(\omega-\omega_{\mathrm{TLS}}^i\right)+\frac{\gamma_{\mathrm{TLS}}^i}{2}} - \frac{\left(i\Omega_{AB} - \sum_{i=1}^{N}\left(\frac{2g_i^2}{-i\left(\omega-\omega_{\mathrm{TLS}}^i\right)+\frac{\gamma_{\mathrm{TLS}}^i}{2}}\right)\right)^2}{-i(\omega-\omega_A)+\kappa_A+\gamma_A-\sum_{i=1}^{N}\frac{2Sg_i^2}{-i\left(\omega-\omega_{\mathrm{TLS}}^i\right)+\frac{\gamma_{\mathrm{TLS}}^i}{2}}}}, \tag{B15}$$

and

$$S_{41} = \frac{\sqrt{\kappa_{Bx}\kappa_B}}{L_{B,+}} - \frac{L_{AB,+}\left(L_{B,+}\sqrt{\kappa_B\kappa_A} - L_{AB,+}\sqrt{\kappa_B\kappa_{Bx}}\right)}{L_{B,+}\left(L_{B,+}L_{A,+} - L_{AB,+}^2\right)} + \frac{\sqrt{\kappa_{Ax}\kappa_A} - \frac{\sqrt{\kappa_{Ax}}L_{AB,+}\sqrt{\kappa_{Ax}\kappa_{Bx}}}{L_{B,+}}}{L_{A,+} - \frac{L_{AB,+}^2}{L_{B,+}}}. \tag{B16}$$

Reducing the calculation to equal coupling and photon decay rates for each resonator, $\kappa_A = \kappa_B = \kappa_r$ and $\gamma_A = \gamma_B = \gamma_r$, and assuming no (cross-)coupling to the unintended transmission line, $\kappa_{Ax} = \kappa_{Bx} = 0$, the transmission properties of this four-port system coupling to a single TLS through the $a + b$ field [where the plus sign is taken from Eq. (B4)] is

$$S_{43} = S_{21} = 1 - \kappa_A \frac{-i(\omega-\omega_r') + \kappa_r + \gamma_r}{-(\omega-\omega_r')^2 + (\kappa_r+\gamma_r)^2 - \left(i\Omega_{AB} - \frac{\tanh\left(\frac{\hbar\omega}{2k_BT}\right)g^2}{-i(\omega-\omega_{\mathrm{TLS}})+\frac{\gamma_{\mathrm{TLS}}}{2}}\right)^2 - 2i(\kappa_r+\gamma_r)(\omega-\omega_r')}, \tag{B17}$$

where

$$\omega_r' = \omega_r - \frac{g^2}{\omega - \omega_{\mathrm{TLS}} + i\frac{\gamma_{\mathrm{TLS}}}{2}}.$$

Figure 11 shows additional transmission curves taken from Eq. (B17), which can be compared to Fig. 4(f). Similarly, coupling to a single TLS through the $a - b$ field can be obtained.

### 2. Standard-coupled two-resonator

Considering the standard-coupled two-resonator with a Hamiltonian of

$$H_{\mathrm{sys}} = \hbar\omega_A a^\dagger a + \hbar\omega_B b^\dagger b + \hbar\Omega_{AB}(b^\dagger a + a^\dagger b) + \varepsilon_{\mathrm{TLS}}\sigma^z \tag{B18}$$

$$- i\hbar g_A(\sigma_A^+ a + \sigma_A^- a^\dagger) - i\hbar g_B(\sigma_B^+ b + \sigma_B^- b^\dagger), \tag{B19}$$

and assuming that $g_A = g_B = g$, we obtain

$$S_{43} = S_{21} = 1 - \kappa_A \frac{-i(\omega-\omega_r') + \kappa_r + \gamma_r}{-(\omega-\omega_r')^2 + (\kappa_r+\gamma_r)^2 + \Omega_{AB}^2 - 2i(\kappa_r+\gamma_r)(\omega-\omega_r')}. \tag{B20}$$

### 3. Coherent drive in the Hamiltonian (treatment of the many-photon case)

We consider the case of incoming coherent radiation from the left-hand side of the transmission line, i.e., port 1 or 3. The presence of such coherent drive is accounted for by an effective Hamiltonian

$$H = H_{\mathrm{sys}} + H_d, \tag{B21}$$

where the drive appears as a term $H_d = i\hbar J a^\dagger + \mathrm{H.c.}$ and $J = \sqrt{\Gamma_{\mathrm{ext}}^a}A(t)$, and $\Gamma_{\mathrm{ext}}^a = \kappa_A$. This form is derived by assuming that $\langle a_{1,\mathrm{in}}(t)\rangle = A(t)$ and $\langle a_{2,\mathrm{in}}(t)\rangle = \langle b_{3,\mathrm{in}}(t)\rangle = \langle b_{4,\mathrm{in}}(t)\rangle = 0$. The interaction of a single TLS with the resonators can be

described by the Jaynes-Cummings Hamiltonian in a frame rotating at the pump frequency $\omega_p$:

$$H = \hbar(\omega_p - \omega_A)a^\dagger a + \hbar(\omega_p - \omega_B)b^\dagger b + \frac{\hbar(\omega_p - \omega_{\mathrm{TLS}})}{2}\sigma_z + \hbar\Omega_{AB}(b^\dagger a + a^\dagger b) - i\hbar g(\sigma^-(a^\dagger + b^\dagger) - \sigma^+(a+b)) + i\hbar J(a^\dagger - a). \tag{B22}$$

The corresponding dissipation can be described by the Lindblad master equation [61]:

$$\frac{d\rho}{dt} = -i\hbar[H_{\mathrm{sys}}, \rho] + \Gamma_{\downarrow\uparrow}(n_{\mathrm{th}} + 1)\mathcal{D}_\sigma(\rho) + \frac{\Gamma_\phi}{2}\mathcal{D}_{\sigma z}(\rho) + \Gamma_{\downarrow\uparrow} n_{\mathrm{th}}\mathcal{D}_{\sigma^\dagger}(\rho) + \Gamma^a_{\mathrm{ext}}\mathcal{D}_a(\rho) + \Gamma^b_{\mathrm{ext}}\mathcal{D}_b(\rho), \tag{B23}$$

where the occupation number of the TLS is $n_{\mathrm{th}} = 1/(e^{\hbar\omega/kT} - 1)$, the damping of resonators $A$ and $B$ in the absence of TLSs is $\Gamma^a_{\mathrm{ext}} = \kappa_A$ and $\Gamma^b_{\mathrm{ext}} = \kappa_B$, the TLS dephasing rate is $\Gamma_\phi$, its rate at zero temperature $\Gamma_{\downarrow\uparrow}$, and $\mathcal{D}_A(\rho) = A\rho A^\dagger - 1/2(A^\dagger A\rho + \rho A^\dagger A)$. Using $\langle A\rangle = \mathrm{Tr}\,\langle A\rho\rangle$ and $(d/dt)\,\langle A\rangle = \mathrm{Tr}\,\langle A(d/dt)\rho\rangle$, we can compute the Maxwell-Bloch equations,

$$\frac{d\,\langle a\rangle}{dt} = \left(-i(\omega_p - \omega_a) - \frac{\Gamma^a_{\mathrm{ext}}}{2}\right)\langle a\rangle + g_a\,\langle\sigma\rangle + J, \tag{B24}$$

$$\frac{d\,\langle b\rangle}{dt} = \left(-i(\omega_p - \omega_b) - \frac{\Gamma^b_{\mathrm{ext}}}{2}\right)\langle b\rangle + g_b\,\langle\sigma\rangle\,, \tag{B25}$$

$$\frac{d\,\langle\sigma\rangle}{dt} = (-i(\omega_p - \omega_{\mathrm{TLS}}) - \Gamma_2)\,\langle\sigma\rangle + g_a\,\langle a\sigma_z\rangle + g_b\,\langle b\sigma_z\rangle\,, \tag{B26}$$

$$\frac{d\,\langle\sigma_z\rangle}{dt} = -2g_a\left(\left\langle a^\dagger\sigma\right\rangle + \left\langle a\sigma^\dagger\right\rangle\right) - 2g_b\left(\left\langle b^\dagger\sigma^-\right\rangle + \left\langle b\sigma^+\right\rangle\right) - \Gamma_1\left(\langle\sigma_z\rangle - \langle\sigma_z\rangle_{\mathrm{th}}\right), \tag{B27}$$

where we define $\Gamma_2 = (\Gamma_{\downarrow\uparrow}/2)(1 + 2n_{\mathrm{th}}) + \Gamma_\phi$, $\Gamma_1 = \Gamma_{\downarrow\uparrow}(1 + 2n_{\mathrm{th}})$, and $\langle\sigma_z\rangle_{\mathrm{th}} = -1/(1 + 2n_{\mathrm{th}}) = -\tanh(\hbar\omega/2k_BT)$. To transform this system [Eqs. (B24)–(B27)] into a closed set of equations, we neglect the correlations and factorize the products $\langle a\sigma_z\rangle = \langle a\rangle\,\langle\sigma_z\rangle$, $\left\langle a^\dagger\sigma_z\right\rangle = \left\langle a^\dagger\right\rangle\langle\sigma_z\rangle$, $\langle b\sigma_z\rangle = \langle b\rangle\,\langle\sigma_z\rangle$, and $\left\langle b^\dagger\sigma_z\right\rangle = \left\langle b^\dagger\right\rangle\langle\sigma_z\rangle$. We first determine the solution for the cavity field, $\langle a\rangle$ and $\langle b\rangle$, using the approximations $\langle a\rangle = \alpha + \delta\alpha(t)e^{-i(\omega_p - \omega_a)t}$, $\langle b\rangle = \beta + \delta\beta(t)e^{-i(\omega_p - \omega_b)t}$, $\langle\sigma\rangle = \sigma_0 + \delta\sigma(t)e^{-i(\omega_p - \omega_{\mathrm{TLS}})t}$, and $\langle\sigma_z\rangle = \sigma_{z0}$, where $\delta\alpha(t)$, $\delta\beta(t)$, and $\delta\sigma(t)$ are slowly varying complex functions [61]. The equations for the stationary components are as follows:

$$0 = \left(-i(\omega_p - \omega_a) - \frac{\Gamma^a_{\mathrm{ext}}}{2}\right)\alpha + g_a\sigma_0 - i\Omega_{AB}\beta + J, \tag{B28}$$

$$0 = \left(-i(\omega_p - \omega_b) - \frac{\Gamma^b_{\mathrm{ext}}}{2}\right)\beta + g_b\sigma_0 - i\Omega_{AB}\alpha, \tag{B29}$$

$$0 = (-i(\omega_p - \omega_{\mathrm{TLS}}) - \Gamma_2)\sigma_0 + g_a\alpha\sigma_{z0} + g_b\beta\sigma_{z0}, \tag{B30}$$

$$0 = -2g_a(\alpha^*\sigma_0 + \alpha\sigma_0^*) - 2g_b(\beta^*\sigma_0 + \beta\sigma_0^*) - \Gamma_1\left(\sigma_{z0} - \langle\sigma_z\rangle_{\mathrm{th}}\right). \tag{B31}$$

Grouping terms by terms related to $\alpha$ and $\beta$, one finds that

$$\sigma_0 = \frac{g_a\alpha\sigma_{z0} + g_b\beta\sigma_{z0}}{i(\omega_p - \omega_{\mathrm{TLS}}) + \Gamma_2}. \tag{B32}$$

The solution for the outfield is obtained from the boundary conditions $a_{1,(2),\mathrm{out}} = \sqrt{\Gamma^a_{\mathrm{ext}}}a - a_{2,(1),\mathrm{in}}$ by inserting the assumed form of the input field $\langle a_{1,\mathrm{in}}(t)\rangle = A(t)$. From Eq. (B29) and by replacing $\sigma_0$ from Eq. (B32), we have

$$0 = \left(-i(\omega_p - \omega_b) - \frac{\Gamma^b_{\mathrm{ext}}}{2}\right)\beta + \frac{g_b g_a \alpha \sigma_{z0} + g_b g_b \beta \sigma_{z0}}{i(\omega_p - \omega_{\mathrm{TLS}}) + \Gamma_2} - i\Omega_{AB}\alpha, \tag{B33}$$

$$0 = \left(-i(\omega_p - \omega_b) - \frac{\Gamma^b_{\mathrm{ext}}}{2} + \frac{g_b g_b \sigma_{z0}}{i(\omega_p - \omega_{\mathrm{TLS}}) + \Gamma_2}\right)\beta + \frac{g_b g_a \alpha \sigma_{z0}}{i(\omega_p - \omega_{\mathrm{TLS}}) + \Gamma_2} - i\Omega_{AB}\alpha \tag{B34}$$

$$-\left(-i(\omega_p - \omega_b) - \frac{\Gamma^b_{\mathrm{ext}}}{2} + \frac{g_b g_b \sigma_{z0}}{i(\omega_p - \omega_{\mathrm{TLS}}) + \Gamma_2}\right)\beta = \frac{g_b g_a \alpha \sigma_{z0}}{i(\omega_p - \omega_{\mathrm{TLS}}) + \Gamma_2} - i\Omega_{AB}\alpha \tag{B35}$$

$$-\left(-i(\omega_p - \omega_b) - \frac{\Gamma^b_{\mathrm{ext}}}{2} + \frac{g_b g_b \sigma_{z0}}{i(\omega_p - \omega_{\mathrm{TLS}}) + \Gamma_2}\right)\beta = \left(\frac{g_b g_a \sigma_{z0}}{i(\omega_p - \omega_{\mathrm{TLS}}) + \Gamma_2} - i\Omega_{AB}\right)\alpha. \tag{B36}$$

Finally, we obtain

$$\beta = \frac{-\frac{g_b g_a \sigma_{z0}}{i(\omega_p - \omega_{\mathrm{TLS}}) + \Gamma_2} + i\Omega_{AB}}{\left(-i(\omega_p - \omega_b) - \frac{\Gamma^b_{\mathrm{ext}}}{2} + \frac{g_b g_b \sigma_{z0}}{i(\omega_p - \omega_{\mathrm{TLS}}) + \Gamma_2}\right)}\alpha \tag{B37}$$

To proceed to the output fields, we next substitute the solution for $\beta$ from Eq. (B37) into Eq. (B28):

$$0 = \left(-i\left(\omega_p - \omega_a\right) - \frac{\Gamma^a_{\mathrm{ext}}}{2} + \frac{g_a g_a \sigma_{z0}}{i(\omega_p - \omega_{\mathrm{TLS}}) + \Gamma_2}\right)\alpha + \left(-i\Omega_{AB} + \frac{g_a g_b \sigma_{z0}}{i(\omega_p - \omega_{\mathrm{TLS}}) + \Gamma_2}\right)\beta + J, \tag{B38}$$

$$\left(i\left(\omega_p - \omega_a\right) + \frac{\Gamma^a_{\mathrm{ext}}}{2} - \frac{g_a g_a \sigma_{z0}}{i(\omega_p - \omega_{\mathrm{TLS}}) + \Gamma_2}\right)\alpha + \left(i\Omega_{AB} - \frac{g_a g_b \sigma_{z0}}{i(\omega_p - \omega_{\mathrm{TLS}}) + \Gamma_2}\right)\beta = J, \tag{B39}$$

$$\left(i(\omega_p - \omega_a) + \frac{\Gamma^a_{\mathrm{ext}}}{2} - \frac{g_a g_a \sigma_{z0}}{i(\omega_p - \omega_{\mathrm{TLS}}) + \Gamma_2}\right)\alpha + \left(i\Omega_{AB} - \frac{g_a g_b \sigma_{z0}}{i(\omega_p - \omega_{\mathrm{TLS}}) + \Gamma_2}\right)\frac{-\frac{g_b g_a \sigma_{z0}}{i(\omega_p - \omega_{\mathrm{TLS}}) + \Gamma_2} + i\Omega_{AB}}{\left(-i(\omega_p - \omega_b) - \frac{\Gamma^b_{\mathrm{ext}}}{2} + \frac{g_b g_b \sigma_{z0}}{i(\omega_p - \omega_{\mathrm{TLS}}) + \Gamma_2}\right)}\alpha = J, \tag{B40}$$

$$\left[\left(i(\omega_p - \omega_a) + \frac{\Gamma^a_{\mathrm{ext}}}{2} - \frac{g_a g_a \sigma_{z0}}{i(\omega_p - \omega_{\mathrm{TLS}}) + \Gamma_2}\right) + \frac{\left(i\Omega_{AB} - \frac{g_a g_b \sigma_{z0}}{i(\omega_p - \omega_{\mathrm{TLS}}) + \Gamma_2}\right)\left(i\Omega_{AB} - \frac{g_a g_b \sigma_{z0}}{i(\omega_p - \omega_{\mathrm{TLS}}) + \Gamma_2}\right)}{\left(-i(\omega_p - \omega_b) - \frac{\Gamma^b_{\mathrm{ext}}}{2} + \frac{g_b g_b \sigma_{z0}}{i(\omega_p - \omega_{\mathrm{TLS}}) + \Gamma_2}\right)}\right]\alpha = \sqrt{\Gamma^a_{\mathrm{ext}}}a_{1,\mathrm{in}}. \tag{B41}$$

The solution for the resonator $\alpha$ field is

$$\alpha = \frac{\sqrt{\Gamma^a_{\mathrm{ext}}}}{\left[\left(i(\omega_p - \omega_a) + \frac{\Gamma^a_{\mathrm{ext}}}{2} - \frac{g_a g_a \sigma_{z0}}{i(\omega_p - \omega_{\mathrm{TLS}}) + \Gamma_2}\right) + \frac{\left(i\Omega_{AB} - \frac{g_a g_b \sigma_{z0}}{i(\omega_p - \omega_{\mathrm{TLS}}) + \Gamma_2}\right)^2}{\left(-i(\omega_p - \omega_b) - \frac{\Gamma^b_{\mathrm{ext}}}{2} + \frac{g_b g_b \sigma_{z0}}{i(\omega_p - \omega_{\mathrm{TLS}}) + \Gamma_2}\right)}\right]}a_{1,\mathrm{in}}. \tag{B42}$$

Using this result, one can find transmission and reflection using the boundary condition $a_{2,\mathrm{out}} = \sqrt{\Gamma^a_{\mathrm{ext}}}a - a_{1,\mathrm{in}}$. The transmission, $S_{21} = a_{2,\mathrm{out}}/a_{1,\mathrm{in}}$, can be written as

$$S_{21} = 1 - \frac{\Gamma^a_{\rm ext}}{\left[\left(i(\omega_p - \omega_a) + \frac{\Gamma^a_{\rm ext}}{2} - \frac{g_a g_a \sigma_{z0}}{i(\omega_p - \omega_{\rm TLS}) + \Gamma_2}\right) + \frac{\left(i\Omega_{AB} - \frac{g_a g_b \sigma_{z0}}{i(\omega_p - \omega_{\rm TLS}) + \Gamma_2}\right)^2}{\left(-i(\omega_p - \omega_b) - \frac{\Gamma^b_{\rm ext}}{2} + \frac{g_b g_b \sigma_{z0}}{i(\omega_p - \omega_{\rm TLS}) + \Gamma_2}\right)}\right]}, \tag{B43}$$

where

$$\sigma_{z0} = \langle \sigma_z \rangle_{\rm th} \left[1 - \frac{\Gamma_2^2 \bar{n}/n_s}{(\omega_{\rm TLS} - \omega_p) + \Gamma_2^2(1 + \bar{n}/n_s)}\right], \tag{B44}$$

$\bar{n} = |A(t)|^2$ is the mean photon number in the cavity, and $n_s^{-1} = 4g^2/\Gamma_1\Gamma_2$ the number of photons required to saturate the TLS transition.

### 4. Correlation amplitude

TLS $(1/f)$ frequency noise causes noise in resonator transmission (e.g., $S_{21}$), where the transmission changes in phase and amplitude. The noise is mainly seen in a particular direction in $I$-$Q$ space as fluctuations in $[\mathrm{Re}(S_{21}(f_{0A})), \mathrm{Im}(S_{21}(f_{0A}))]$ and $[\mathrm{Re}(S_{21}(f_{0B})), \mathrm{Im}(S_{21}(f_{0B}))]$, which are tangent to the complex transmission plot, where we use Eq. (B14) to define the quadratures $[Q'_A, I'_A]$ and $[Q'_B, I'_B]$ shown in Fig. 5(c). As in a standard KID, the fluctuation quadrature is thus a frequency noise. However, now we have two input frequencies and two TLS noise sources.

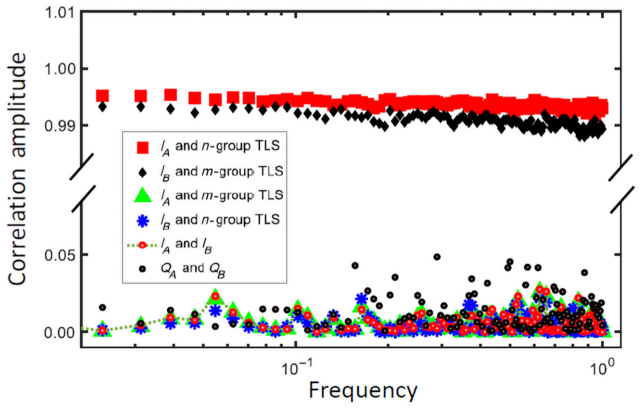


FIG. 12. The correlation amplitude $C_{xy}$ between the noise quantities: $1/f$-noise TLS frequencies and resonator transmission quadratures ($I_A$, $Q_A$, $I_B$, and $Q_B$). The $1/f$ noise sources from $m$-group TLSs and $n$-group TLSs are not correlated, as there is no significant TLS-TLS coupling mechanism. There is near-perfect noise correlation between $I_A$ and $n$-group TLSs and between $I_B$ and $m$-group TLSs. There is no significant normalized correlation between resonator quadratures $I_A$ and $I_B$ because the noise fluctuations occur as an $m$- or $n$-group TLS source on a corresponding resonator quadrature $I_A$ or $I_B$. This implies that noise is not significantly correlated through the resonator-resonator coupling. $Q_A$ and $Q_B$ have slightly larger normalized correlation amplitudes but this is of no consequence because these quadratures have small noise powers.

The TLSs induce noise in the resonators, where $I'_A$ and $I'_B$ in Fig. 5(c) are defined to be tangent to the transmission versus frequency plot near the probe frequencies $[f_A, f_B]$. In Fig. 9, we show the correlation amplitude (the normalized cross-spectral density),

$$C_{xy} = \frac{S_v^{xy}}{(S_v^{xx} S_v^{yy})^{1/2}}, \tag{B45}$$

between different quadratures and TLS groups. Here, $x$ and $y$ are the different possible aforementioned TLS- and quadrature-noise types. $S_v^{xy}$ is the cross-spectral density between $x$ and $y$, and $S_v^{xx}$ and $S_v^{yy}$ are the autospectral density of $x$ and $y$, respectively. The result plotted in Fig. 9 shows that the $1/f$ noise on each mode and its own TLS fluctuations are highly correlated but the noise induced on the measurement quadratures of the two resonator modes is uncorrelated.


[1] P. K. Day, H. G. LeDuc, B. A. Mazin, A. Vayonakis, and J. Zmuidzinas, A broadband superconducting detector suitable for use in large arrays, Nature **425**, 817 (2003).

[2] B. A. Mazin, Ph.D. thesis, California Institute of Technology, 2004.

[3] J. Gao, J. Zmuidzinas, B. A. Mazin, H. G. LeDuc, and P. K. Day, Noise properties of superconducting coplanar waveguide microwave resonators, Appl. Phys. Lett. **90**, 102507 (2007).

[4] O. Noroozian, J. Gao, J. Zmuidzinas, H. G. LeDuc, and B. A. Mazin, Two-level system noise reduction for microwave kinetic inductance detectors, AIP Conf. Proc. **1185**, 148 (2009).

[5] S. Schlör, J. Lisenfeld, C. Müller, A. Bilmes, A. Schneider, D. P. Pappas, A. V. Ustinov, and M. Weides, Correlating decoherence in transmon qubits: Low frequency noise by single fluctuators, Phys. Rev. Lett. **123**, 190502 (2019).

[6] O. Dial, D. T. McClure, S. Poletto, J. M. Gambetta, D. W. Abraham, J. M. Chow, and M. Steffen, Bulk and surface loss in superconducting transmon qubits, Supercond. Sci. Technol. **29**, 044001 (2016).

[7] J. Burnett *et al.*, Evidence for interacting two-level systems from the $1/f$ noise of a superconducting resonator, Nat. Commun. **5**, 4119 (2014).

[8] J. Gao, M. Daal, A. Vayonakis, S. Kumar, J. Zmuidzinas, B. Sadoulet, B. A. Mazin, P. K. Day, and H. G. Leduc, Experimental evidence for a surface distribution of two-level systems in superconducting lithographed microwave resonators, Appl. Phys. Lett. **92**, 152505 (2008).

[9] C. R. H. McRae, H. Wang, J. Gao, M. R. Vissers, T. Brecht, A. Dunsworth, D. P. Pappas, and J. Mutus, Materials loss measurements using superconducting microwave resonators, Rev. Sci. Instrum. **91**, 091101 (2020).

[10] P. R. Maloney *et al.*, MUSIC for sub/millimeter astrophysics, Proc. SPIE **v7741**, 124 (2010).

[11] A. Monfardini *et al.*, A dual-band millimeter-wave kinetic inductance camera for the IRAM 30 m telescope, Astrophys. J. **194**, 24 (2011).

[12] N. Galitzki *et al.*, Millimeter, submillimeter, and far-infrared detectors and instrumentation for astronomy VIII, Int. Soc. Opt. Photonics **9914**, 108 (2016).

[13] E. L. Wright, G. Hinshaw, and C. L. Bennett, Producing megapixel cosmic microwave background from differential radiometer data, Astrophys. J. Lett. **v.458**, L53 (1996).

[14] D. Maino, C. Burigana, K. M. Górski, N. Mandolesi, and M. Bersanelli, Removing $1/f$ noise stripes in cosmic microwave background anisotropy observations, Astron. Astrophys. **v.387**, 356 (2002).

[15] N. J. Miller, D. T. Chuss, T. A. Marriage, E. J. Wollack, J. W. Appel, C. L. Bennett, J. Eimer, T. Essinger-Hileman, D. J. Fixsen, K. Harrington, S. H. Moseley, K. Rostem, E. R. Switzer, and D. J. Watts, Recovery of large angular scale CMB polarization for instruments employing variable-delay polarization modulators, Astrophys. J. **818**, 151 (2016).

[16] S. Hailey-Dunsheath, R. M. J. Janssen, J. Glenn, C. M. Bradford, J. Perido, J. Redford, and J. Zmuidzinas, Kinetic inductance detectors for the Origins Space Telescope, J. Astron. Telescopes, Instrum. Syst. **7**, 011015 (2021).

[17] B. R. Johnson, D. Flanigan, M. H. Abitbol, P. A. R. Ade, S. Bryan, H.-M. Cho, R. Datta, P. Day, S. Doyle, K. Irwin, G. Jones, D. Li, P. Mauskopf, H. McCarrick, J. McMahon, A. Miller, G. Pisano, Y. Song, H. Surdi, and C. Tucker, Development of multi-chroic MKIDs for next-generation CMB polarization studies, J. Low Temp. Phys. **193**, 103 (2018).

[18] J. van Rantwijk, M. Grim, D. van Loon, S. Yates, A. Baryshev, and J. Baselmans, Multiplexed readout for 1000-pixel arrays of microwave kinetic inductance detectors, IEEE Transactions on Microwave Theory and Techniques **64**, 1876 (2016).

[19] C. Müller, J. Lisenfeld, A. Shnirman, and S. Poletto, Interacting two-level defects as sources of fluctuating high-frequency noise in superconducting circuits, Phys. Rev. B **92**, 035442 (2015).

[20] J. Kelly *et al.*, Scalable *in situ* qubit calibration during repetitive error detection, Phys. Rev. A **94**, 032321 (2016).

[21] J. M. Martinis, K. B. Cooper, R. McDermott, M. Steffen, M. Ansmann, K. D. Osborn, K. Cicak, S. Oh, D. P. Pappas, R. W. Simmonds, and C. C. Yu, Decoherence in Josephson qubits from dielectric loss, Phys. Rev. Lett. **95**, 210503 (2005).

[22] J. Gao and J. Zmuidzinas, Noise properties of superconducting coplanar waveguide microwave resonators, Appl. Phys. Lett. **90**, 102507 (2007).

[23] J. Gao, M. Daal, J. M. Martinis, A. Vayonakis, J. Zmuidzinas, B. Sadoulet, B. A. Mazin, P. K. Day, and H. G. Leduc, A semiempirical model for two-level system noise in superconducting microresonators, Appl. Phys. Lett. **92**, 212504 (2008).

[24] L. Faoro and L. B. Ioffe, Interacting tunneling model for two-level systems in amorphous materials and its predictions for their dephasing and noise in superconducting microresonators, Phys. Rev. B **91**, 014201 (2015).

[25] M. Schechter, P. Nalbach, and A. L. Burin, Nonuniversality and strongly interacting two-level systems in glasses at low temperatures, New J. Phys. **20**, 063048 (2018).

[26] Yoni Shalibo, Ya'ara Rofe, David Shwa, Felix Zeides, Matthew Neeley, John M. Martinis, and Nadav Katz, Lifetime and coherence of two-level defects in a Josephson junction, Phys. Rev. Lett. **105**, 177001 (2010).

[27] R. W. Simmonds, K. M. Lang, D. A. Hite, S. Nam, D. P. Pappas, and J. M. Martinis, Decoherence in Josephson phase qubits from junction resonators, Phys. Rev. Lett. **93**, 077003 (2004).

[28] M. Steffen, M. Sandberg, and S. Srinivasan, Recent research trends for high coherence quantum circuits, Supercond. Sci. Technol. **30**, 030301 (2017).

[29] Y. Chu, C. Axline, C. Wang, T. Brecht, Y. Y. Gao, L. Frunzio, and R. J. Schoelkopf, Suspending superconducting qubits by silicon micromachining, Appl. Phys. Lett. **109**, 112601 (2016).

[30] J. Burnett *et al.*, Evidence for interacting two-level systems from the $1/f$ noise of a superconducting resonator, Nat. Commun. **5**, 4119 (2014).

[31] C. Neill, A. Megrant, R. Barends, Yu Chen, B. Chiaro, J. Kelly, J. Y. Mutus, P. J. J. O'Malley, D. Sank, J. Wenner, T. C. White, Y. Yin, A. N. Cleland, and J. M. Martinis, Fluctuations from edge defects in superconducting resonators, Appl. Phys. Lett. **103**, 072601 (2013).

[32] S. J. C. Yates, J. Bueno, A. Endo, A. M. Baryshev, L. Ferrari, V. Murugesan, D. J. Thoen, and J. J. A. Baselmans, On the design and performance of very large MKID arrays, Proc. SPIE, v. 11453, Millimeter, Submillimeter, and Far-Infrared Detectors and Instrumentation for Astronomy X; 114530C (2020).

[33] P. J. De Visser, *Quasiparticle Dynamics in Aluminium Superconducting Microwave Resonators* (Delft University of Technology, Delft, Netherlands, 2014).

[34] B. A. Mazin, K. O'Brien, S. McHugh, B. Bumble, D. Moore, S. Golwala, and J. Zmuidzinas, ARCHONS: A highly multiplexed superconducting optical to near-IR camera, SPIE Proceedings, v. 7735, Ground-based and Airborne Instrumentation for Astronomy III; 773518 (2010).

[35] S. Doyle, P. Mauskopf, J. Naylon, A. Porch, and C. Duncombe, Lumped element kinetic inductance detectors, J. Low Temp. Phys. **151**, 530 (2008).

[36] H. McCarrick, G. Jones, B. R. Johnson, M. H. Abitbol, P. A. R. Ade, S. Bryan, P. Day, T. Essinger-Hileman, D. Flanigan, H. G. Leduc, M. Limon, P. Mauskopf, A. Miller, and C. Tucker, Design and performance of dual-polarization lumped-element kinetic inductance detectors for millimeter-wave polarimetry, A&A **610**, A45 (2018).

[37] H. Paik and K. D. Osborn, Reducing quantum-regime dielectric loss of silicon nitride for superconducting quantum circuits, Appl. Phys. Lett. **96**, 072505 (2010).
[38] M. R. Vissers, J. Hubmayr, M. Sandberg, S. Chaudhuri, C. Bockstiegel, and J. Gao, Frequency-tunable superconducting resonators via nonlinear kinetic inductance, Appl. Phys. Lett. **107**, 062601 (2015).
[39] S. J. Weber, K. W. Murch, D. H. Slichter, R. Vijay, and I. Siddiqi, Single crystal silicon capacitors with low microwave loss in the single photon regime, Appl. Phys. Lett. **98**, 172510 (2011).
[40] G. Cataldo, E. J. Wollack, E. M. Barrentine, A. D. Brown, S. H. Moseley, and K. U-Yen, Analysis and calibration techniques for superconducting resonators, Rev. Sci. Instrum. **86**, 013103 (2015).
[41] C. W. Gardiner and M. J. Collett, Input and output in damped quantum systems: Quantum stochastic differential equations and the master equation, Phys. Rev. A **31**, 3761 (1985).
[42] D. F. Walls and G. Milburn, *Quantum Optics* (Springer-Verlag, Berlin, 2008).
[43] J. M. Fink, M. Göppl, M. Baur, R. Bianchetti, P. J. Leek, A. Blais, and A. Wallraff, Climbing the Jaynes-Cummings ladder and observing its nonlinearity in a cavity QED system, Nature **454**, 315 (2008).
[44] J. M. Fink, R. Bianchetti, M. Baur, M. Göppl, L. Steffen, S. Filipp, P. J. Leek, A. Blais, and A. Wallraff, Dressed collective qubit states and the Tavis-Cummings model in circuit QED, Phys. Rev. Lett. **103**, 083601 (2009).
[45] B. Sarabi, A. N. Ramanayaka, A. L. Burin, F. C. Wellstood, and K. D. Osborn, Cavity quantum electrodynamics using a near-resonance two-level system: Emergence of the Glauber state, Appl. Phys. Lett. **106**, 172601 (2015).
[46] J. Leppäkangas, J. D. Brehm, P. Yang, L. Guo, M. Marthaler, A. V. Ustinov, and M. Weides, Resonance inversion in a superconducting cavity coupled to artificial atoms and a microwave background, Phys. Rev. A **99**, 063804 (2019).
[47] M. Mirzaei, E. M. Barrentine, B. T. Bulcha, G. Cataldo, J. A. Connors, N. Ehsan, T. M. Essinger-Hileman, L. A. Hess, J. W. Mugge-Durum, O. Noroozian, T. M. Oxholm, T. R. Stevenson, E. R. Switzer, C. G. Volpert, and E. J. Wollack, $\mu$-spec spectrometers for the EXCLAIM instrument, Proceedings Volume 11453, Millimeter, Submillimeter, and Far-Infrared Detectors and Instrumentation for Astronomy X; 114530M (2020).
[48] J. Baselmans, S. J. C. Yates, R. Barends, Y. J. Y. Lankwarden, J. R. Gao, H. Hoevers, and T. M. Klapwijk, Noise and sensitivity of aluminum kinetic inductance detectors for sub-mm astronomy, J. Low Temp. Phys. **151**, 524 (2008).
[49] J. A. Schlaerth, Ph.D. thesis, University of Colorado at Boulder, 2010.
[50] D. Flanigan, Ph.D. thesis, Columbia University, New York, 2018.
[51] P. J. De Visser, Ph.D. thesis, Delft University of Technology, Delft, Netherlands, 2015.
[52] T. R. Stevenson, Limits on the sensitivity of spherical gravitational wave detectors and on the accuracy of reconstructed signals, Phys. Rev. D **56**, 564 (1997).
[53] J. Perido, J. Glenn, P. Day, A. Fyhrie, H. Leduc, J. Zmuidzinas, and C. McKenney, Extending KIDs to the mid-IR for future space and suborbital observatories, J. Low Temp. Phys. **199**, 696 (2020).
[54] O. Noroozian, E. M. Barrentine, T. R. Stevenson, A. D. Brown, S. H. Moseley, E. Wollack, K. M. Pontoppidan, K. U-Yen, and V. Mikula, Photon-Counting Kinetic Inductance Detectors (KID) for Far/Mid-Infrared Space Spectroscopy with the Origins Space Telescope (OST), American Astronomical Society, AAS Meeting 231, id. 447.01 (2018).
[55] A. E. Lowitz, E. M. Barrentine, S. R. Golwala, and P. T. Timbie, A comparison of fundamental noise in kinetic inductance detectors and transition edge sensors for millimeter-wave applications, J. Low Temp. Phys. **176**, 504 (2014).
[56] L. Grunhaupt, N. Maleeva, S. T. Skacel, M. Calvo, F. Levy-Bertrand, A. V. Ustinov, H. Rotzinger, A. Monfardini, G. Catelani, and I. M. Pop, Loss mechanisms and quasiparticle dynamics in superconducting microwave resonators made of thin-film granular aluminum, Phys. Rev. Lett. **121**, 117001 (2018).
[57] M. S. Khalil, M. J. A. Stoutimore, F. C. Wellstood, and K. D. Osborn, An analysis method for asymmetric resonator transmission applied to superconducting devices, J. Appl. Phys. **111**, 054510 (2012).
[58] B. Sarabi, A. N. Ramanayaka, A. L. Burin, F. C. Wellstood, and K. D. Osborn, Projected dipole moments of individual two-level defects extracted using circuit quantum electrodynamics, Phys. Rev. Lett. **116**, 167002 (2016).
[59] S. Hunklinger and A. K. Raychaudhuri, Thermal and elastic anomalies in glasses at low temperatures, Prog. Low Temp. Phys. **9**, 344 (1986).
[60] J. Classen, C. Enss, C. Bechinger, G. Weiss, and S. Hunklinger, Low frequency acoustic and dielectric measurements on glasses, Ann. Phys. **506**, 315335 (1994).
[61] T. Capelle *et al.*, Probing a two-level system bath via the frequency shift of an off-resonantly driven cavity, Phys. Rev. Appl. **13**, 034022 (2020).